Structural and Multidisciplinary Optimization manuscript No.
(will be inserted by the editor)

A new stabilisation approach for level-set based topology optimisation of hyperelastic materials

Rogelio Ortigosa · Jesús Martínez-Frutos · Antonio J. Gil · David Herrero-Pérez

Received: date / Accepted: date

Abstract This paper introduces a novel computational approach for level-set based topology optimisation of hyperelastic materials at large strains. This, to date, is considered an unresolved open problem in topology optimisation due to its extremely challenging nature. Two computational strategies have been proposed to address this problem. The first strategy resorts to an arc-length in the pre-buckling region of intermediate TO iterations where numerical difficulties arise (associated with nucleation, disconnected elements, etc.), and is then continued by a novel regularisation technique in the post-buckling region. In the second strategy, the regularisation technique is used for the entire loading process at each TO iteration.

The success of both rests on the combination of three distinct key ingredients. First, the nonlinear equilibrium equations of motion are solved in a consistent incrementally linearised fashion by splitting the design load into a number of load increments. Second, the resulting linearised tangent elasticity tensor is stabilised (regularised) in order to prevent its loss of positive definiteness and, thus, avoid the loss of convexity of the discrete tangent operator. Third, and with the purpose of avoiding excessive numerical stabilisation, a scalar degradation function is applied on the regularised linearised elasticity tensor, based on a novel regularisation indicator field. The robustness and applicability of this new methodological approach is thoroughly demonstrated through an ample spectrum of challenging numerical examples, ranging from benchmark two-dimensional (plane stress) examples to larger scale three-dimensional applications. Crucially, the performance of all the designs has been tested at a postprocessing stage without adding any source of artificial stiffness. Specifically, an arc-length Newton-Raphson method has been employed in conjunction with a ratio of the material parameters for void and solid regions of 10^{-12}.

Keywords Topology optimisation · level-set · Nonlinear elasticity · Polyconvexity

Rogelio Ortigosa
Computational Mechanics & Scientific Computing Group, Technical University of Cartagena , Campus Muralla del Mar, 30202 Cartagena (Murcia), Spain
E-mail: rogelio.ortigosa@upct.es
This work started whilst at the previous affiliation: Zienkiewicz Centre for Computational Engineering, College of Engineering, Swansea University, Bay Campus, SA1 8EN, United Kingdom

Jesús Martínez-Frutos
Computational Mechanics & Scientific Computing Group, Technical University of Cartagena , Campus Muralla del Mar, 30202 Cartagena (Murcia), Spain
E-mail: jesus.martinez@upct.es

Antonio J. Gil
Zienkiewicz Centre for Computational Engineering, College of Engineering Swansea University, Swansea, United Kingdom
E-mail: a.j.gil@swansea.ac.uk

David Herrero-Pérez
Computational Mechanics & Scientific Computing Group, Technical University of Cartagena , Campus Muralla del Mar, 30202 Cartagena (Murcia), Spain
E-mail: david.herrero@upct.es

1 Introduction

Soft materials, such as rubbery polymers, capable of undergoing large deformations, have experienced fast industrial development over the last decade. For instance, a paradigm switch is expected in the field of robotics,

where conventional hard robots will be progressively replaced by the emerging field of soft robotics (comprised of soft and hard materials with a strategic combination of maximum elasticity modulus of 1 GPa) (Rus and Tolley, 2015; Wehner et al, 2016; Wallin et al, 2018; Gursel, 2018). Soft robots possess desirable biomimetic and dextrous features even superseding those of natural muscles and represent an emerging approach for the design of new prosthetics. Furthermore, their softness allow for safer interactions with humans. An additional appealing feature of these materials is the suitability for their rapid prototyping by means of cutting-edge 3D printing technologies (Wallin et al, 2018).

Since the pioniering work of Bendsoe and Kikuchi (Bendsoe and Kikuchi, 1988), the scientific field of structural Topology Optimisation (TO) has been extraordinarily prolific. According to (Sigmund and Maute, 2013), topology optimisation methods can be broadly classified into: density-based methods (Bendsøe, 1989; Zhou and Rozvany, 1991), level-set methods (Allaire et al, 2004; Wang et al, 2003), phase field methods (Burger and Stainko, 2006; Takezawa et al, 2010), topological derivative methods (Norato et al, 2007; Sokolowski and Zochowski, 1999) and evolutionary approaches (Munk et al, 2015). Based on these techniques, scientists have pushed the boundaries of topology optimisation to an unprecedented level, with applications in a variety of problems, from nanophotonics design (Jensen and Sigmund, 2011) to aircraft and aerospace structural design (Zhu et al, 2016; Aage et al, 2017).

Despite the matured and consolidated stage of topology optimisation in the linear elastic regime, where very small displacements/strains are expected to occur, this is unfortunately not the case for the topology optimisation of soft materials undergoing large displacements/strains. One of the main reasons for this long standing open problem stems from the numerical difficulties which arise when trying to satisfy exactly the *state equations* (equilibrium equations). In essence, the underlying reason for these numerical difficulties resides in the co-existence of two crucial factors: (i) the loss of convexity of the invariant-based representation of the strain energy, which ultimately yields loss of positive definiteness of the tangent operator; (ii) the presence of low and intermediate density regions (in the case of the SIMP[1] method Wang et al (2014)) or the nucleation process that occur when initiating the algorithm from a generic seed (in the case of the level-set method Chen et al (2017)). The combination of these two factors poses a serious limitation to the robust applicability of well-established techniques such as the arc-length method (Bonet et al (2016b)), which were specifically designed to surpass limit points and to successfully track snap-through and snap-back equilibrium path-types. As a result, researchers in the field have been working in order to develop methodological approaches capable of alleviating all of these numerical difficulties. Although in a different context, these difficulties are also present in the field of nonlinear continuum mechanics for problems characterised by a saddle point nature (Bonet et al, 2016b).

On another front, the presence of disconnected structural elements (islands) is not a feature exclusive of the level-set method. (Bruns and Tortorelli, 2003) proposed element removal and re-introduction strategies in order to deal with this issue within the context of the SIMP method. Furthermore, density-based methods can exhibit an additional source of numerical instability related to the presence of low and intermediate densities (notice that in level-set TO, densities are 1 or 0, and can only adopt an intermediate value on the boundary of the solid). Although many authors have proposed techniques to alleviate this (Lahuerta et al (2013), Wang et al (2014), Liu et al (2017)), low and intermediate densities still pose a challenge for the robustness of density-based TO at large strains (specially at low volume fractions), as they are responsible for the development of very low or even negative Jacobians, which seriously hamper numerical robustness.

There exists an extremely valuable body of work in topology optimisation of soft materials, specially using the SIMP approach. The additive hyperelasticity technique (Liu et al, 2017) was created in order to alleviate the numerical difficulties associated with the presence of low and intermediate density regions. Very recently, the authors in (Lahuerta et al, 2013) proposed the use of polyconvex strain energy functions in conjunction with an *ad-hoc* relaxation aiming to stabilise excessively distorted elements of the finite element mesh, mainly associated also with low and intermediate regions. More recently, an original interpolation scheme for strain energy of the material was proposed by (Wang et al, 2014) in order to alleviate these numerical difficulties. All of the aforementioned works adopted density based optimisation methods. With regards to the level-set based topology optimisation method, only a reduced number of works address this problem. In this case, additional numerical difficulties may appear during the nucleation process. When starting from an initial generic seed, slender and even disconnected structural elements might develop before a final stable shape is obtained. (Ha and Cho, 2008) applied the level-set method to topology optimisation of hyperelastic structures with moderate finite deformations. They proposed an explicit representation of the boundary using a Delaunay

[1] Solid Isotropic Material with Penalisation

triangulation scheme and a hyperelastic material law to circumvent the convergence difficulty in nonlinear response analysis due to the inaccurate tangent stiffness when using an ersatz material approach. Recently, the authors in Chen et al (2017) have shown that the consideration of an initial seed, obtained from a preliminary optimisation using linear analysis, can reduce the instabilities associated with the nucleation process up to a certain magnitude of the design load. Additionally, when rather large deformation arises, a continuation approach was used to update the material properties of the weak material from 0.01 to 0.001 times those of the solid material. Very recently, in (Geiss et al, 2018) a level-set approach together with the extended finite element method (XFEM) has been combined with density-based topology optimisation to describe the evolving multi-material design problem in the optimisation process. A finite deformation hyperelastic thermo-mechanical model is used together with a higher order XFEM scheme to accurately predict the behaviour of nonlinear slender structures during the design evolution.

A common feature in above approaches is the *relaxation* (regularisation) of the Lagrangian whose stationary point is sought[2]. In this paper, we follow a similar idea and seek the relaxation of the Lagrangian through a careful regularisation of the state equations, within the context of level-set topology optimisation. The new approach aims to circumvent the numerical difficulties associated with the original problem (loss of convexity and nucleation), by a combination of three key ingredients. First, the nonlinear equilibrium equations of motion are solved in a consistent incrementally linearised fashion by splitting the design load into a number of load increments. Second, at each load increment, the resulting linearised tangent elasticity tensor is stabilised (regularised) in order to prevent its loss of positive definiteness and, thus, avoid the loss of convexity of the discrete tangent operator. Third, and with the purpose of avoiding excessive numerical stabilisation, a scalar degradation function is introduced, based on a novel regularisation indicator field, in order to penalise the regularised linearised elasticity tensor. The proposed methodology alleviates numerical instabilities emerging during the nucleation process associated with the level-set based topology optimisation. In that regard, the robustness of the proposed methodology is not dependant upon the choice of the material properties of the void region or upon the choice of an initial seed. Crucially, the performance of all the designs obtained in the numerical examples section has been tested at a postprocessing stage without adding any source of artificial stiffness. Specifically, a standard arc-length Newton-Raphson based technique has been employed in conjunction with a stiffness of 10^{-12} times the stiffness of solid elements for void elements. This enables to verify the level of relaxation introduced in the original Lagrangian and the reliability of the final designs.

Notice that consideration of buckling has not been incorporated at this stage (either in the objective function or as a constraint). Nonetheless, the proposed method enables to obtain final stable designs for considerably large design loads hence, yielding very large critical load factors. Thus, the numerical strategy proposed indirectly enhances the buckling response of the optimal designs obtained.

The outline of this paper is as follows: Section 2 describes the necessary elements of nonlinear continuum mechanics. Section 3 describes succinctly the minimisation setting within the context of nonlinear elasticity. Section 4 presents the new incrementally regularised methodology proposed. Finally, Section 5 shows a series of numerical examples in order to illustrate the robustness and applicability of the new proposed methodology. Section 6 provides some concluding remarks. Finally, Appendix A shows how to particularise the theory on nonlinear continuum mechanics in Section 2 to the case of plane stress.

2 Nonlinear continuum mechanics

2.1 Kinematics of a continuum

Let us consider the motion of a continuum with reference or material configuration $\Omega_0 \in \mathbb{R}^3$ of boundary $\partial\Omega_0$ with outward normal $\boldsymbol{N}$ (see Figure 2.1). After the motion, the continuum occupies a deformed or spatial configuration $\Omega \in \mathbb{R}^3$ of boundary $\partial\Omega$ with outward normal $\boldsymbol{n}$. The mapping $\boldsymbol{\phi}(\boldsymbol{X}) \in \mathbb{R}^3$ links a particle from the reference configuration $\boldsymbol{X} \in \Omega_0$ to a deformed configuration $\boldsymbol{x} \in \Omega$ according to $\boldsymbol{x} = \boldsymbol{\phi}(\boldsymbol{X}) = \boldsymbol{X} + \boldsymbol{u}$, with $\boldsymbol{u}$ the displacement field. Associated with $\boldsymbol{\phi}(\boldsymbol{X})$, it is possible to define the two-point[3] deformation gradient tensor $\boldsymbol{F}$ as

$$\boldsymbol{F} = \boldsymbol{\nabla}_0 \boldsymbol{\phi}(\boldsymbol{X}) = \boldsymbol{I} + \boldsymbol{\nabla}_0 \boldsymbol{u}; \qquad F_{iI} = \frac{\partial \phi_i}{\partial X_I}, \tag{1}$$

where $\boldsymbol{\nabla}_0$ denotes the material gradient operator and $\boldsymbol{I}$ represents the second order identity tensor. Associated with $\boldsymbol{F}$ (1) it is possible to define two extra kinematic

[2] The well-known augmented Lagrangian method (Bonet et al, 2016b) is a prototypical example of these approaches.

[3] Lower (upper) case indices are used to refer to the spatial (material) configuration.

strain measures, namely its co-factor $\boldsymbol{H}$ and its Jacobian J as

$$J = \det \boldsymbol{F}; \qquad \boldsymbol{H} = J\boldsymbol{F}^{-T}. \tag{2}$$

The three entities above $\{\boldsymbol{F}, \boldsymbol{H}, J\}$ represent the kinematic measures which transform differential length, area and volume elements from the reference configuration, namely $\{d\boldsymbol{X}, d\boldsymbol{A}, dV\}$ to the spatial configuration, namely $\{d\boldsymbol{x}, d\boldsymbol{a}, dv\}$, according to $\{d\boldsymbol{x} = \boldsymbol{F}d\boldsymbol{X}, d\boldsymbol{a} = \boldsymbol{H}d\boldsymbol{X}, dv = JdV\}$ (see Figure 2.1 for a visual interpretation of the three kinematic measures). Alternative but equivalent expressions for $\boldsymbol{H}$ and J to those in (2) are (de Boer (1982); Bonet et al (2015b, 2016a, 2015a))

$$\boldsymbol{H} = \frac{1}{2}\boldsymbol{F} \times \boldsymbol{F}; \qquad J = \frac{1}{3}\boldsymbol{H} : \boldsymbol{F}, \tag{3}$$

where the tensor cross product operation $\times$ between two second order tensors $\boldsymbol{A} \in \mathbb{R}^{3\times 3}$ and $\boldsymbol{B} \in \mathbb{R}^{3\times 3}$ reads as $(\boldsymbol{A} \times \boldsymbol{B})_{iI} = \mathcal{E}_{ijk}\mathcal{E}_{IJK}A_{jJ}B_{kK}$, where $\mathcal{E}_{ijk}$ (and $\mathcal{E}_{IJK}$) represents the third order alternating tensor.

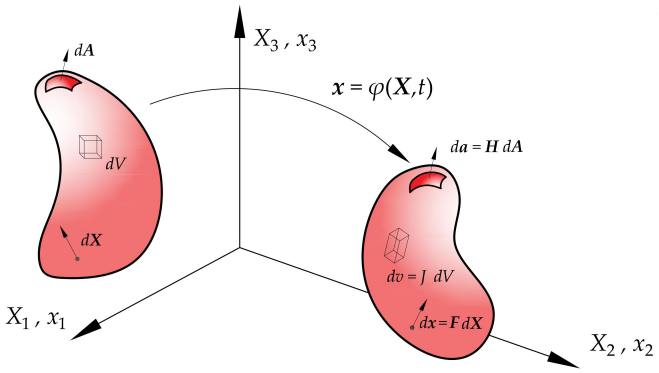

Fig. 1 The three kinematic measures: $\{\boldsymbol{F}, \boldsymbol{H}, J\}$.

2.2 Governing equations in nonlinear continuum mechanics

The partial differential equations and associated boundary conditions governing the motion of the continuum Ω_0 described in Section 2.1 can be written under a Lagrangian formalism as

$$\begin{aligned} \mathrm{DIV}\boldsymbol{P} + \boldsymbol{f}_0 &= \boldsymbol{0}; && \text{in } \Omega_0; \\ \boldsymbol{P}\boldsymbol{N} &= \boldsymbol{t}_0; && \text{on } \partial_N\Omega_0; \\ \boldsymbol{\phi} &= \bar{\boldsymbol{\phi}}; && \text{on } \partial_{\boldsymbol{\phi}}\Omega_0, \end{aligned} \tag{4}$$

where (4) represent the classical equilibrium equations, $\boldsymbol{f}_0$ represents the body force per unit undeformed volume Ω_0 and $\boldsymbol{t}_0$, the traction force per unit undeformed area applied on $\partial_N\Omega_0 \subset \partial\Omega_0$. Furthermore, $\partial_{\boldsymbol{\phi}}\Omega_0$ represents the portion of the boundary $\partial\Omega_0$ where Dirichlet boundary conditions are applied on $\boldsymbol{\phi}$, with $\partial_N\Omega_0 \cup \partial_{\boldsymbol{\phi}}\Omega_0 = \partial\Omega_0$ and $\partial_N\Omega_0 \cap \partial_{\boldsymbol{\phi}}\Omega_0 = \emptyset$. In addition, $\boldsymbol{P}$ represents the first Piola-Kirchhoff stress tensor and the local conservation of angular momentum leads to the well-known tensor condition $\boldsymbol{P}\boldsymbol{F}^T = \boldsymbol{F}\boldsymbol{P}^T$. Finally, DIV $(\bullet)$ represents the material divergence operator, i.e. $(\mathrm{DIV}\boldsymbol{P})_i = \frac{\partial P_{iJ}}{\partial X_J}$.

2.3 Constitutive model: polyconvex hyperelasticity

In order to close the system of equations in (4), a constitutive equation relating the first Piola-Kirchhoff stress tensor $\boldsymbol{P}$ and the deformation gradient tensor $\boldsymbol{\nabla}_0\boldsymbol{\phi}$ is needed. In the case of reversible elasticity, this is achieved through the introduction of a strain energy e per unit undeformed volume $e = e(\boldsymbol{\nabla}_0\boldsymbol{\phi})$. We consider in this work polyconvex strain energy functionals, namely

$$e\left(\boldsymbol{\nabla}_0\boldsymbol{\phi}\right) = W\left(\mathcal{V}\right); \qquad \mathcal{V} = \{\boldsymbol{F}, \boldsymbol{H}, J\}, \tag{5}$$

where W is a convex function with respect to the extended set $\mathcal{V}$ of kinematic measures. A commonly used polyconvex constitutive model is the so-called Mooney-Rivlin model, defined as

$$\begin{aligned} W &= \frac{\mu_1}{2}II_{\boldsymbol{F}} + \frac{\mu_2}{2}II_{\boldsymbol{H}} + f(J); \\ f(J) &= \frac{\lambda}{2}\left(J-1\right)^2 - \left(\mu_1 + 2\mu_2\right)\ln J - \frac{3}{2}\left(\mu_1 + \mu_2\right), \end{aligned} \tag{6}$$

with $II_{\boldsymbol{A}} = \boldsymbol{A} : \boldsymbol{A} = A_{iI}A_{iI}$ and where the material parameters $\{\mu_1, \mu_2, \lambda\}$ are related to the Young's modulus and Poisson ratio in the origin, namely E and ν, respectively, as

$$\begin{aligned} \mu_1 + \mu_2 &= \frac{E}{2\left(1+\nu\right)}; \\ \lambda - 2(\mu_1 + \mu_2) &= \frac{E\nu}{\left(1+\nu\right)\left(1-2\nu\right)}. \end{aligned} \tag{7}$$

Let $\delta\boldsymbol{a}$ and $\Delta\boldsymbol{a}$ represent virtual and incremental variations of a given vector field $\boldsymbol{a}$. Thus, the directional derivative of the strain energy e with respect to $\delta\boldsymbol{\phi}$ yields the first Piola-Kirchhoff stress tensor $\boldsymbol{P}$ as

$$De[\delta\boldsymbol{\phi}] - \boldsymbol{P} : \boldsymbol{\nabla}_0\delta\boldsymbol{\phi} = \boldsymbol{0} \Rightarrow \boldsymbol{P} = \partial_{\boldsymbol{\nabla}_0\boldsymbol{\phi}}e\left(\boldsymbol{\nabla}_0\boldsymbol{\phi}\right), \tag{8}$$

where the symbol $\partial_{\boldsymbol{A}}\boldsymbol{B}$ represents the partial derivative of $\boldsymbol{B}$ with respect to $\boldsymbol{A}$. The fourth order elasticity

tensor $\boldsymbol{\mathcal{C}}$ results from the computation of the second directional derivative of the strain energy as

$$D^2e[\delta\boldsymbol{\phi};\Delta\boldsymbol{\phi}] = \boldsymbol{\nabla}_0\delta\boldsymbol{\phi} : \boldsymbol{\mathcal{C}} : \boldsymbol{\nabla}_0\Delta\boldsymbol{\phi}; \qquad \boldsymbol{\mathcal{C}} = \partial^2_{\boldsymbol{\nabla}_0\boldsymbol{\phi}\boldsymbol{\nabla}_0\boldsymbol{\phi}} e\left(\boldsymbol{\nabla}_0\boldsymbol{\phi}\right). \tag{9}$$

Remark 1*. Alternative expressions for the first Piola-Kirchoff stress tensor* $\boldsymbol{P}$ *and the elasticity tensor* $\boldsymbol{\mathcal{C}}$ *can be obtained when considering the extended representation of the strain energy, namely* $W(\mathcal{V})$*. Indeed, as shown in Bonet et al (2016a, 2015a,b),* $\boldsymbol{P}$ *can also be expressed as*

$$\boldsymbol{P} = \partial_{\boldsymbol{F}}W + \partial_{\boldsymbol{H}}W \bigtimes \boldsymbol{F} + \partial_J W\boldsymbol{H}. \tag{10}$$

Similarly, as shown in Bonet et al (2016a, 2015a,b), the elasticity tensor $\boldsymbol{\mathcal{C}}$ *can be expressed as*

$$\begin{aligned}\boldsymbol{\mathcal{C}} &= \partial^2_{\boldsymbol{F}\boldsymbol{F}}W + \boldsymbol{F}\bigtimes\partial^2_{\boldsymbol{H}\boldsymbol{H}}W\bigtimes\boldsymbol{F} + \partial^2_{JJ}W\boldsymbol{H}\otimes\boldsymbol{H}\\ &+ \partial^2_{\boldsymbol{F}J}W\otimes\boldsymbol{H} + \boldsymbol{H}\otimes\partial^2_{J\boldsymbol{F}}W + \partial^2_{\boldsymbol{F}\boldsymbol{H}}W\bigtimes\boldsymbol{F}\\ &+ \boldsymbol{F}\bigtimes\partial^2_{\boldsymbol{H}\boldsymbol{F}}W + \boldsymbol{F}\bigtimes\partial^2_{\boldsymbol{H}J}W\otimes\boldsymbol{H} + \boldsymbol{H}\otimes\partial^2_{J\boldsymbol{H}}W\bigtimes\boldsymbol{F}\\ &+ \boldsymbol{\mathcal{I}}\bigtimes(\partial_{\boldsymbol{H}}W + \partial_J W\boldsymbol{F}),\end{aligned} \tag{11}$$

where

$$\begin{aligned}\mathcal{I}_{iIjJ} &= \delta_{iI}\delta_{jJ};\\ (\boldsymbol{\mathcal{A}}\bigtimes\boldsymbol{A})_{iIjJ} &= \mathcal{A}_{iIpP}\mathcal{E}_{jpq}\mathcal{E}_{JPQ}A_{qQ};\\ (\boldsymbol{A}\bigtimes\boldsymbol{\mathcal{A}})_{iIjJ} &= \mathcal{A}_{qQjJ}\mathcal{E}_{ipq}\mathcal{E}_{IPQ}A_{pQ},\end{aligned} \tag{12}$$

for any $\boldsymbol{\mathcal{A}}\in\mathbb{R}^{3\times3\times3\times3}$ *and* $\boldsymbol{A}\in\mathbb{R}^{3\times3}$ *and* δ_{ij} *denotes the* ij*-th component of the Kronecker Delta tensor. The reader is referred to Ortigosa et al (2015); Ortigosa and Gil (2017) for a detailed derivation of* $\boldsymbol{\mathcal{C}}$ *in* (11)*.*

□

3 Optimisation

3.1 The minimisation problem

As described in Section 2.2, the boundary of Ω_0 is decomposed as $\partial\Omega_0 = \partial_{\boldsymbol{\phi}}\Omega_0\cup\partial_N\Omega_0$. The boundary $\partial_N\Omega_0$ can be further decomposed as $\partial_N\Omega_0 = \partial_t\Omega_0\cup\partial_o\Omega_0$, where $\partial_t\Omega_0$ and $\partial_o\Omega_0$ represent the Neumann portion of the boundary where $\boldsymbol{t}_0\neq\boldsymbol{0}$ and $\boldsymbol{t}_0=\boldsymbol{0}$, respectively. Therefore, $\partial_o\Omega_0$ is the only part of the boundary $\partial\Omega_0$ which can be evolved through the optimisation process, changing at each topology optimisation (TO) iteration. Let the evolving continuum Ω_0 be contained within a working (computational) domain D, i.e. $\Omega_0\subset D$. We introduce the set of admissible shapes $\mathcal{U}_{\text{ad}}$ subjected to the volume constraint V^*, i.e.

$$\mathcal{U}_{\text{ad}} = \{\Omega_0\subset D : |\Omega_0| = V^*\}; \qquad |\Omega_0| = \int_{\Omega_0} dV. \tag{13}$$

The mimisation problem considered can be written as

$$(P_1)\quad \begin{cases}\min\limits_{\Omega_0\in\mathcal{U}_{\text{ad}}} \mathcal{J}\left(\Omega_0,\boldsymbol{u}\right),\\ \text{s.t. State equations (1), (4) and } (8)_b\end{cases} \tag{14}$$

where $\mathcal{J}\left(\Omega_0,\boldsymbol{u}\right)$ represents the objective function to be minimised and with $\boldsymbol{u}\in H^1(\Omega_0;\mathbb{R}^3)$. In this work, the *end* compliance is chosen as the objective function, defined as

$$\mathcal{J}\left(\Omega_0,\boldsymbol{u}\right) = \int_{\Omega_0}\boldsymbol{f}_0\cdot\boldsymbol{u}\,dV + \int_{\partial_t\Omega_0}\boldsymbol{t}_0\cdot\boldsymbol{u}\,dA. \tag{15}$$

In the context of large deformations it is customary to solve the equilibrium constraint (4) in an incremental manner (i.e. $n=0\ldots N-1$). Hence, the external forces ($\boldsymbol{f}_0$ and $\boldsymbol{t}_0$ in (4)) are applied incrementally, i.e. controlling their magnitude by the incremental load factor λ_{n+1} at load increment $n+1$, such that $\lambda_{n+1}=(n+1)/N$, with N the total number of load increments. The Lagrangian functional associated with the minimisation problem in (14) can be written within this incremental setting as

$$\begin{aligned}\mathcal{L}\left(\Omega_0,\boldsymbol{\mathcal{U}},\boldsymbol{\mathcal{P}},\ell_1\right) &= \mathcal{J}\left(\Omega_0,\boldsymbol{u}_N\right)\\ &+ \sum_{n=0}^{N-1}\mathit{\Pi}\left(\Omega_0,\boldsymbol{u}_{n+1},\boldsymbol{p}_{n+1}\right)\\ &+ \ell_1\left(|\Omega_0|-V^*\right) + \frac{\gamma_1}{2}\left(|\Omega_0|-V^*\right)^2;\\ \mathit{\Pi}\left(\Omega_0,\boldsymbol{u}_{n+1},\boldsymbol{p}_{n+1}\right) &= -\int_{\Omega_0}\boldsymbol{P}(\boldsymbol{F}_{n+1}) : \boldsymbol{\nabla}_0\boldsymbol{p}_{n+1}\,dV\\ &+ \lambda_{n+1}\left(\int_{\Omega_0}\boldsymbol{p}_{n+1}\cdot\boldsymbol{f}_0\,dV\right.\\ &+ \left.\int_{\partial_t\Omega_0}\boldsymbol{p}_{n+1}\cdot\boldsymbol{t}_0\,dA\right),\end{aligned} \tag{16}$$

where $\boldsymbol{\mathcal{U}}=\{\boldsymbol{u}_1,...,\boldsymbol{u}_{n+1},...,\boldsymbol{u}_N\}$ ($\boldsymbol{u}_n\in H^1(\Omega_0;\mathbb{R}^3)$) represent the set of incremental solutions of the equilibrium constraint (4), $\boldsymbol{\mathcal{P}}=\{\boldsymbol{p}_1,...,\boldsymbol{p}_{n+1},...,\boldsymbol{p}_N\}$ ($\boldsymbol{p}_n\in H^1_0(\Omega_0;\mathbb{R}^3)$) represent their adjoint state counterparts and ℓ_1 and γ_1, the Lagrange multiplier and the penalty parameter, respectively, enforcing the volume constraint (see (13)) at convergence.

3.2 Stationary conditions of the augmented Lagrangian $\mathcal{L}$

The stationary conditions of the Lagrangian $\mathcal{L}$ (16) yield the optimality conditions of (P_1) (14). The stationary condition of $\mathcal{L}$ with respect to $\delta\boldsymbol{p}_{n+1}\in H^1_0(\Omega_0;\mathbb{R}^3)$

yields

$$D\mathcal{L}[\delta\boldsymbol{p}_{n+1}] = -\int_{\Omega_0} \boldsymbol{P}(\boldsymbol{F}_{n+1}) : \boldsymbol{\nabla}_0 \delta\boldsymbol{p}_{n+1}\, dV + \lambda_{n+1}\left(\int_{\Omega_0} \boldsymbol{f}_0 \cdot \delta\boldsymbol{p}_{n+1}\, dV + \int_{\partial_t\Omega_0} \boldsymbol{t}_0 \cdot \delta\boldsymbol{p}_{n+1}\, dA\right) = 0. \tag{17}$$

Equation (17) represents the so-called weak form of the equilibrium equations (4). For a given Ω_0, solution of (17) enables to obtain the displacement field $\boldsymbol{u}_{n+1}$ which is compliant with the Dirichlet boundary conditions and that it is in equilibrium with the external loads $\lambda_{n+1}\boldsymbol{f}_0$ and $\lambda_{n+1}\boldsymbol{t}_0$, at every load increment $n+1$ and every TO iteration. Furthermore, the stationary condition of $\mathcal{L}$ with respect to $\delta\boldsymbol{u}_{n+1} \in H_0^1(\Omega_0;\mathbb{R}^3)$ for the specific case when $n = N-1$ yields

$$D\mathcal{L}[\delta\boldsymbol{u}_N] = -\int_{\Omega_0} \boldsymbol{\nabla}_0\boldsymbol{p}_N : \boldsymbol{\mathcal{C}}(\boldsymbol{F}_N) : \boldsymbol{\nabla}_0\delta\boldsymbol{u}_N\, dV + \int_{\Omega_0} \boldsymbol{f}_0 \cdot \delta\boldsymbol{u}_N\, dV + \int_{\partial_t\Omega_0} \boldsymbol{t}_0 \cdot \delta\boldsymbol{u}_N\, dA = 0. \tag{18}$$

Equation (18) permits to obtain the adjoint state at load increment N, e.g. $\boldsymbol{p}_N$. Furthermore, the stationary condition of $\mathcal{L}$ with respect to $\delta\boldsymbol{u}_{n+1} \in H_0^1(\Omega_0;\mathbb{R}^3)$ for the case when $n \neq N-1$ yields

$$D\mathcal{L}[\delta\boldsymbol{u}_{n+1}] = -\int_{\Omega_0} \boldsymbol{\nabla}_0\boldsymbol{p}_{n+1} : \boldsymbol{\mathcal{C}}(\boldsymbol{F}_{n+1}) : \boldsymbol{\nabla}_0\delta\boldsymbol{u}_{n+1}\, dV = 0, \tag{19}$$

which yields the trivial solution $\boldsymbol{p}_{n+1} = \boldsymbol{0}$ (if $n \neq N-1$ and if the problem is well-posed). Therefore, technically speaking, only the adjoint problem corresponding to the last load increment N needs to be solved for (e.g. equation (18)). It is worth noticing that stationary conditions (17) and (18) do not coincide, except for the particular case of linear elasticity. Therefore, problem (P_1) (14) is not strictly speaking a self-adjoint problem in the general nonlinear case, i.e. $\boldsymbol{u}_N \neq \boldsymbol{p}_N$.

3.3 Shape derivative of the augmented Lagrangian $\mathcal{L}$

A velocity field $\boldsymbol{\vartheta} \in W^{1,\infty}(D;\mathbb{R}^3)$, subjected to $\vartheta_N := (\boldsymbol{\vartheta}\cdot\boldsymbol{N}) = 0$ on $\partial_{\boldsymbol{\phi}}\Omega_0 \cup \partial_t\Omega_0$, is introduced in order to account for the evolution of the boundary $\partial_o\Omega_0$. The shape derivative of $\mathcal{L}$, namely $D\mathcal{L}[\boldsymbol{\vartheta}]$, is the key ingredient to define a descent direction which permits to evolve the boundary $\partial_o\Omega_0$ at every TO iteration.

Remark 5. *For the functional $\mathcal{F}$ defined as*

$$\mathcal{F} = \int_{\Omega_0} f\, dV, \tag{20}$$

it can be shown (see Reference Allaire (2006)) that $D\mathcal{F}[\boldsymbol{\vartheta}]$ can be obtained as

$$D\mathcal{F}[\boldsymbol{\vartheta}] = \int_{\partial_o\Omega_0} \vartheta_N f\, dA. \tag{21}$$

□

The shape derivative of $\mathcal{L}$ (16) can now be shown to be

$$\begin{aligned} D\mathcal{L}[\boldsymbol{\vartheta}] &= \int_{\partial_o\Omega_0} \vartheta_N v\, dA; \\ v &= \boldsymbol{f}_0\cdot\boldsymbol{u}_N \\ &\quad + \sum_{n=0}^{N-1}\left(\lambda_{n+1}\boldsymbol{f}_0\cdot\boldsymbol{p}_{n+1} - \boldsymbol{P}(\boldsymbol{F}_{n+1}) : \boldsymbol{\nabla}_0\boldsymbol{p}_{n+1}\right) \\ &\quad + \ell_1 + \gamma_1\left(|\Omega_0(\boldsymbol{\vartheta})| - V^*\right) \\ &= \boldsymbol{f}_0\cdot(\boldsymbol{u}_N + \lambda_N\boldsymbol{p}_N) - \boldsymbol{P}(\boldsymbol{F}_N) : \boldsymbol{\nabla}_0\boldsymbol{p}_N \\ &\quad + \ell_1 + \gamma_1\left(|\Omega_0(\boldsymbol{\vartheta})| - V^*\right), \end{aligned} \tag{22}$$

where use of $\boldsymbol{p}_{n+1} = \boldsymbol{0}$ (if $n \neq N-1$) has been made of in (22) (see (19)). In the case where $\boldsymbol{f}_0 = \boldsymbol{0}$, v (22) simplifies to

$$v = -\boldsymbol{P}(\boldsymbol{F}_N) : \boldsymbol{\nabla}_0\boldsymbol{p}_N + \ell_1 + \gamma_1\left(|\Omega_0| - V^*\right). \tag{23}$$

3.4 Numerical solution of (P_1) via the level-set method

Following the original idea by (Osher and Sethian, 1988) and subsequently applied in the context of shape optimisation (Sethian and Wiegmann (2000); Wang et al (2003); Allaire et al (2004)), the level-set method is used to *capture* the evolving domain Ω_0. For this, a pseudo-time parameter $\tau = \tau_0 \ldots \tau_m$ is introduced, where τ is associated with a series of discrete topology optimisation iterations. Thus, the initial configuration of the continuum can be evolved in pseudo-time (i.e. $\Omega_0(\tau)$) throughout an optimisation process from the initial iteration at τ_0 ($\Omega_0(\tau_0)$) passing through an intermediate iteration at τ_i ($\Omega_0(\tau_i)$) and converging at τ_m ($\Omega_0(\tau_m)$) (see Figure 3.4). In the level-set method, the evolving domain $\Omega_0(\tau)$ is described through the zero level-set of the function $\psi = \psi(\boldsymbol{X}(\tau),\tau)$ defined on the working domain D as follows

$$\forall \boldsymbol{X} \in D,\ \forall \tau \in (0,T),\ \begin{cases} \psi(\boldsymbol{X},\tau) < 0; & \text{if } \boldsymbol{X} \in \Omega_0(\tau); \\ \psi(\boldsymbol{X},\tau) = 0; & \text{if } \boldsymbol{X} \in \partial_o\Omega_0(\tau); \\ \psi(\boldsymbol{X},\tau) > 0; & \text{if } \boldsymbol{X} \notin \bar{\Omega}_0(\tau). \end{cases}$$

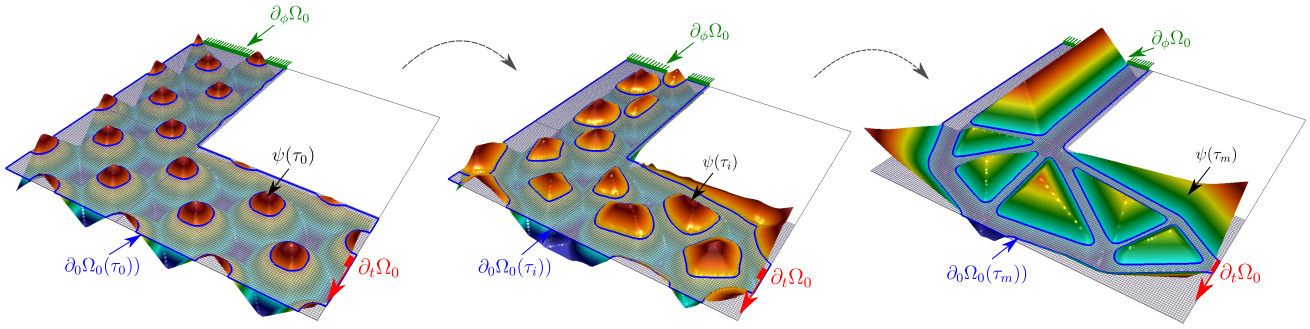

Fig. 2 Evolution of the domain $\Omega_0(\tau)$ throughout the TO process at the initial iteration $\tau = 0$ (left), at intermediate iteration $\tau = i$ (center) and at the final iteration $\tau = m$ (right). $\Omega_0(\tau)$ corresponds to the portion of the (L-shaped) working domain D where the level-set function $\psi(\tau)$ adopts negative values. It can be seen that the boundaries $\partial_\varphi\Omega_0$ and $\partial_t\Omega_0$ remain unaltered.

(24)

Let $\Omega_0(\tau)$ evolve with a velocity $\boldsymbol{\vartheta}(\boldsymbol{X}(\tau),\tau) \in D$. Differentiation of the level-set equation $\psi(\boldsymbol{X}(\tau),\tau) = 0$ with respect to τ yields

$$\partial_\tau\psi + \boldsymbol{\vartheta}\cdot\boldsymbol{\nabla}_0\psi = 0; \quad \tau\in(0,T); \quad \boldsymbol{X}\in\partial_o\Omega_0(\tau). \tag{25}$$

Noting that in the boundary $\partial_o\Omega_0(\tau)$, $\boldsymbol{\vartheta} = \vartheta\boldsymbol{N}$ and $\boldsymbol{\nabla}_0\psi = |\boldsymbol{\nabla}_0\psi|\boldsymbol{N}$, equation (25) can be expressed as

$$\partial_\tau\psi + \vartheta|\boldsymbol{\nabla}_0\psi| = 0; \quad \tau\in(0,T); \quad \boldsymbol{X}\in\partial_o\Omega_0(\tau). \tag{26}$$

Since $\boldsymbol{\vartheta}\in D$, equation (26) needs to be extended to the working domain D as

$$\partial_\tau\psi + \vartheta|\boldsymbol{\nabla}_0\psi| = 0; \quad \tau\in(0,T); \quad \boldsymbol{X}\in D. \tag{27}$$

We recall from (22) that $D\mathcal{L}[\boldsymbol{\theta}]$ can be recast as

$$D\mathcal{L}[\boldsymbol{\vartheta}] = \int_{\partial_0\Omega_0(\tau)} \vartheta_N v\, dA, \tag{28}$$

with $v \in D$ (see (22) and (23)). A descent direction (negative value for $D\mathcal{L}[\boldsymbol{\vartheta}]$ in (28)) is guaranteed if ϑ_N is defined as

$$\vartheta_N = -v. \tag{29}$$

Introduction of (29) into (27) allows to obtain the final form of the *Hamilton-Jacobi* equation, i.e.

$$\partial_\tau\psi - v|\boldsymbol{\nabla}_0\psi| = 0; \quad \tau\in(0,T); \quad \boldsymbol{X}\in D, \tag{30}$$

which is solved using an explicit first order upwind scheme.

Remark 5. *Typically, the stationary conditions* (17)*) and* (18)*) are solved approximately by using the Finite Element method on the whole working domain D (instead of being exactly solved on Ω_0): the so-called ersatz material method is used, whereby the void region $D\backslash\Omega_0$ is filled with a very soft material characterised by a linear constitutive law where the first Piola-Kirchhoff stress tensor, denoted as $\boldsymbol{P}_\varepsilon$, is defined as*

$$\boldsymbol{P}_\varepsilon = \varepsilon\,\boldsymbol{\mathcal{C}}|_{\boldsymbol{\nabla_0\phi=I}} : \boldsymbol{\nabla}_0\boldsymbol{u}; \qquad \varepsilon << 1, \tag{31}$$

where $\boldsymbol{\mathcal{C}}|_{\boldsymbol{\nabla_0\phi=I}}$ represents the elasticity tensor of the material in the domain $\Omega_0(\tau)$ evaluated in the origin (i.e.$\boldsymbol{\nabla}_0\boldsymbol{\phi} = \boldsymbol{I}$).

□

Remark 6. *To avoid singularities, the level-set function is periodically reinitialized. The readers are referred to Allaire et al (2004) for further details.*

□

4 Proposed methodology

4.1 Introduction

One of the major challenges affecting the topology optimisation of structures undergoing large deformations stems from the numerical instabilities which arise when attempting to solve the equilibrium equations in (4). These instabilities are exacerbated during the nucleation that occurs when initiating the level-set method from a starting generic seed. One of the underlying reasons for the development of instabilities is the loss of convexity of the strain energy functional $e(\boldsymbol{\nabla}_0\boldsymbol{\phi})$ or $W(\mathcal{V})$ in (5), leading to loss of positive definiteness of the elasticity tensor $\boldsymbol{\mathcal{C}}$ (in (9) or (11)). Classical post-buckling or equilibrium path-tracking techniques, such as the arc-length method, need to be used in order to guarantee the resolution of (4) (notice that the use of a standard Newton-Raphson method is restricted to the pre-buckling region).

Unfortunately, there are situations where the robustness of these techniques can even be compromised, specially within a TO context, where the following scenarios can occur: (i) situations where the prescribed external loads cannot be in equilibrium with the given

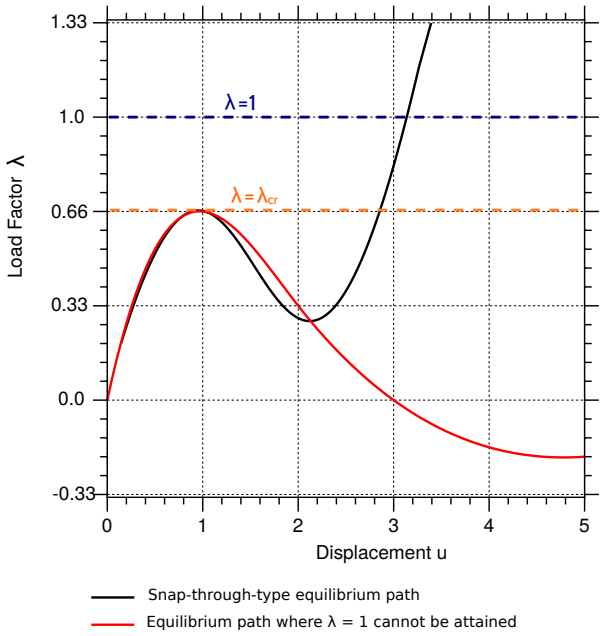

Fig. 3 Arc-length technique

displacement boundary conditions, namely when it is impossible to find a solution to (4) for a loading factor $\lambda = 1$ (this is illustrated in red in Figure 3); (ii) complex equilibrium paths as those resulting during the nucleation process, where very slender and even disconnected structural elements might develop before a final stable shape is obtained.

In these extreme cases, the strict enforcement of the state equations can be relaxed (or weakened) resulting in a regularised Lagrangian potentially capable of circumventing the above difficulties. In principle, this would only need to be done for those TO pseudo-time steps and those load increments where the arc-length method cannot converge. This is elaborated more in detail in Section 4.6. A good example of this methodology is the augmented Lagrangian method typically used in nonlinear continuum mechanics when enforcing kinematic constraints (Bonet et al, 2016b). The objective of the next sections is to present the methodology proposed in this work, with the following key distinct ingredients: (i) a linearised incremental approach for the solution of the equilibrium equations (4) (Section 4.2); (ii) the stabilisation of the elasticity tensor, guaranteeing *ab initio* the stability of (4) (Section 4.3); (iii) a penalisation for excessively (numerically) stabilised regions (Section 4.4). All these ingredients are eventually integrated into a single (regularised) Lagrangian (Section 4.5).

4.2 A consistent incrementally linearised solid mechanics approach

Following the work of (Poya et al, 2016) in the context of mesh generation, we advocate in this work for an approximate linearised incremental resolution of the equilibrium equations (4). This is a valid approximation provided the number of increments controlling the load application is carefully chosen. In this approach, the external forces ($\boldsymbol{f}_0$ and $\boldsymbol{t}_0$ in (4)) are applied incrementally, their magnitude being controlled by an incremental load factor λ_{n+1} at a given load increment $n+1$, such that $\lambda_{n+1} = (n+1)/N$, with N being the total number of load increments. At load increment $n+1$, the strain energy is thus approximated by means of the following Taylor series expansion

$$\begin{aligned} e|_{n+1} \approx e_{\text{inc}}|_{n+1} = e|_n + \boldsymbol{P}|_n : \boldsymbol{\nabla}_0 \Delta\boldsymbol{u}_{n+1} \\ + \frac{1}{2}\boldsymbol{\nabla}_0\Delta\boldsymbol{u}_{n+1} : \boldsymbol{\mathcal{C}}|_n : \boldsymbol{\nabla}_0\Delta\boldsymbol{u}_{n+1}; \\ \Delta\boldsymbol{u}_{n+1} = \boldsymbol{u}_{n+1} - \boldsymbol{u}_n, \end{aligned} \tag{32}$$

with $\boldsymbol{P}|_n$ and $\boldsymbol{\mathcal{C}}|_n$ in (32) obtained as in (8) and (9), i.e.

$$\boldsymbol{P}|_n = \partial_{\boldsymbol{\nabla}_0\boldsymbol{\phi}} e|_n\,; \qquad \boldsymbol{\mathcal{C}}|_n = \partial^2_{\boldsymbol{\nabla}_0\boldsymbol{\phi}\boldsymbol{\nabla}_0\boldsymbol{\phi}} e\big|_n\,. \tag{33}$$

From (32), the approximated first Piola-Kirchhoff stress tensor and the elasticity tensor at load increment $n+1$, namely $\boldsymbol{P}_{n+1}$ and $\boldsymbol{\mathcal{C}}_{n+1}$, respectively, can be obtained as

$$\begin{aligned} \boldsymbol{P}_{n+1} &:= \partial_{\boldsymbol{\nabla}_0\boldsymbol{\phi}} e_{\text{inc}}|_{n+1} = \boldsymbol{P}|_n + \boldsymbol{\mathcal{C}}|_n : \boldsymbol{\nabla}_0\Delta\boldsymbol{u}_{n+1}; \\ \boldsymbol{\mathcal{C}}_{n+1} &:= \partial^2_{\boldsymbol{\nabla}_0\boldsymbol{\phi}\boldsymbol{\nabla}_0\boldsymbol{\phi}} e_{\text{inc}}\big|_{n+1} = \boldsymbol{\mathcal{C}}|_n\,. \end{aligned} \tag{34}$$

4.3 Regularisation/stabilisation of the elasticity tensor

One important ingredient of this work is the stabilisation of local instabilities, characterised by the loss of positive definiteness of the elasticity tensor, which can result in the possible development of global instabilities. We propose a numerical strategy which permits to take advantage of the computational efficiency of the incremental approach described in Section 4.2 whilst allowing for its use beyond the onset of instabilities. In order to accomplish this, we propose a regularisation (stabilisation) of the elasticity tensor at every load increment n, namely $\boldsymbol{\mathcal{C}}|_n$ in (32). This is based on the following additive perturbation of $\boldsymbol{\mathcal{C}}|_n$ through a positive definite elasticity tensor $\Delta\boldsymbol{\mathcal{C}}_{\text{reg}}|_n$ as

$$\begin{aligned} &\boldsymbol{\mathcal{C}}_{\text{reg}}|_n = \boldsymbol{\mathcal{C}}|_n + \Delta\boldsymbol{\mathcal{C}}_{\text{reg}}|_n\,; \\ &\boldsymbol{V} : \boldsymbol{\mathcal{C}}_{\text{reg}}|_n : \boldsymbol{V} \geq 0; \qquad \boldsymbol{V} \in \mathbb{R}^{3\times 3}. \end{aligned} \tag{35}$$

In (35), $\Delta\boldsymbol{\mathcal{C}}_{\text{reg}}|_n$ must be defined such that positive definiteness of the regularised elasticity tensor at each load increment n, namely, $\boldsymbol{\mathcal{C}}_{\text{reg}}|_n$, is satisfied. We investigate in this paper the following simple technique,

$$\Delta\boldsymbol{\mathcal{C}}_{\text{reg}}|_n = (1+\delta)\Gamma\boldsymbol{\mathcal{I}}, \tag{36}$$

with $\Gamma \in \mathbb{R}^+$ such that all the leading minors of the $\boldsymbol{\mathcal{C}}|_n + \Gamma\boldsymbol{\mathcal{I}}$ (and hence $\boldsymbol{\mathcal{C}}_{\text{reg}}|_n$) are positive. Therefore, Γ stabilises the possible loss of convexity of the constitutive model. An iterative bisection algorithm has been implemented in order to find the minimum value of Γ complying with (35). An additional parameter $\delta \in \mathbb{R}^+$ is used in order to prevent the appearance of possible rigid body motions due to the presence of disconnected parts in the structure. For all the simulations shown in this paper, a value $\delta = 10^{-3}$ was used.

4.4 Penalisation of excessive stabilisation

After replacement of $\boldsymbol{\mathcal{C}}|_n$ (32) with $\boldsymbol{\mathcal{C}}_{\text{reg}}|_n$ (35), the following expansion is obtained for the incrementally linearised energy at load increment $n+1$, i.e.

$$\begin{aligned} e_{\text{inc}}|_{n+1} = e|_n + \boldsymbol{P}|_n : \boldsymbol{\nabla}_0\Delta\boldsymbol{u}_{n+1} \\ + \frac{1}{2}\boldsymbol{\nabla}_0\Delta\boldsymbol{u}_{n+1} : \boldsymbol{\mathcal{C}}_{\text{reg}}|_n : \boldsymbol{\nabla}_0\Delta\boldsymbol{u}_{n+1}. \end{aligned} \tag{37}$$

Unfortunately, equation (37) might yield an excessively stiff response of the material due to the regularisation of the elasticity tensor. This could potentially yield a final design for which the first critical load is below the design load. In order to circumvent this, we introduce a regularisation parameter at load increment n, i.e. $s|_n$ as

$$s|_n = \frac{||\,\Delta\boldsymbol{\mathcal{C}}_{\text{reg}}|_n\,||}{||\,\boldsymbol{\mathcal{C}}|_0\,||}, \tag{38}$$

with $||\boldsymbol{\mathcal{A}}|| = \sqrt{\boldsymbol{\mathcal{A}} : \boldsymbol{\mathcal{A}}} = \sqrt{\mathcal{A}_{iIjJ}\mathcal{A}_{iIjJ}}$. Parameter $s|_n$ (38) enables to quantify the violation of condition (35) locally (e.g. at every quadrature point). From (36), $s|_n$ adopts the following expression, namely

$$s = \frac{3\Gamma}{||\,\boldsymbol{\mathcal{C}}|_0\,||}. \tag{39}$$

Inspired by the field of phase-field methods for fracture Hesch et al (2017), we establish an analogy between the regularisation parameter (38) and the damage model used therein in order to characterise the damage state of a material. This enables us to define the degraded incrementally linearised strain energy $\hat{e}_{\text{inc}}|_{n+1}$ by means of the following multiplicative decomposition

$$\hat{e}_{\text{inc}}|_{n+1} = g\,(\,s|_n)\;e_{\text{inc}}|_{n+1}\,; \quad g\,(\,s|_n) \geq 0,\; \forall\; s|_n\,,$$

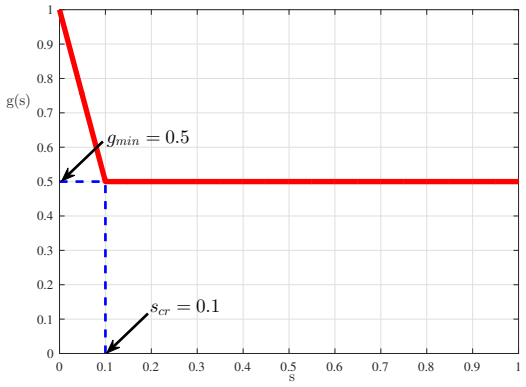

Fig. 4 Graphical representation of the degradation function in (42) with $s_{cr} = 0.1$ and $g_{min} = 0.5$.

(40)

with $\hat{e}_{\text{inc}}|_{n+1}$ defined in (37) and with the function $g\,(\,s|_n)$ playing the role of a degradation function[4]. Specifically, $g(s)$ has been selected monotonically decreasing and satisfying

$$g(0) = 1; \qquad g(s \geq s_{cr}) = g_{min}. \tag{41}$$

In this paper we have investigated the following C^0 definition for $g(s)$ as

$$g(s) = \begin{cases} (g_{min}-1)\frac{s}{s_{cr}} + 1; & s \leq s_{cr} \\ g_{min}; & s > s_{cr} \end{cases}, \tag{42}$$

where g_{min} represents the (user-specified) minimum value that g can take at $s = s_{cr}$ (also user-specified).

From (40), the approximated first Piola-Kirchhoff stress tensor and the elasticity tensor at load increment $n+1$, namely $\boldsymbol{P}_{n+1}$ and $\boldsymbol{\mathcal{C}}_{n+1}$, respectively, can be obtained as

$$\begin{aligned} \boldsymbol{P}_{n+1} &:= \partial_{\boldsymbol{\nabla}_0\boldsymbol{\phi}}\hat{e}_{\text{inc}}|_{n+1} = g\,(\,s|_n)\,(\,\boldsymbol{P}|_n \\ &\qquad + \boldsymbol{\mathcal{C}}_{\text{reg}}|_n : \boldsymbol{\nabla}_0\Delta\boldsymbol{u}_{n+1}\big)\,; \\ \boldsymbol{\mathcal{C}}_{n+1} &:= \partial^2_{\boldsymbol{\nabla}_0\boldsymbol{\phi}\boldsymbol{\nabla}_0\boldsymbol{\phi}}\hat{e}_{\text{inc}}\big|_{n+1} = g\,(\,s|_n)\;\boldsymbol{\mathcal{C}}_{\text{reg}}|_n\,. \end{aligned} \tag{43}$$

In order to illustrate how the proposed methodology works, we carefully select the following simple but insightful numerical experiment. A compressible plane strain isotropic bi-axial deformation state is considered, characterised by the deformation stretch λ, yielding the following expression for the deformation gradient tensor $\boldsymbol{F} = \text{diag}\left(\left[\lambda\;\lambda\;1\right]\right)$. Then, λ is varied within the range $0.1 \leq \lambda \leq 4.4$. The Mooney-Rivlin model in (6) has been considered for this study, with $\mu_1 = 1$, $\mu_2 = 10$

[4] Note how the regularisation parameter featuring in equation (40) is frozen at incremental step n. This removes the nonlinearity altogether and avoids the need to linearise in a Newton-Raphson type manner.

and $\kappa = 10$. Thirty load increments have been considered (i.e. $N = 30$). We compare the incrementally linearised approach in Section 4.2 against the regularisation approach in Section 4.4 for two expressions of the degradation function in (42), with $g_{min} = 1$, $g_{min} = 1/2$ ($s_{cr} = 0.1$). Comparison of Figures 5_a and 5_b clearly illustrates that the regularised approach with no degradation (i.e. $g_{min} = 1$) yields an overestimation of the elasticity tensor. On the contrary, the regularised approach degrades the value of the elasticity tensor. When embedded in a topology optimisation setting, the aim of the degradation function $g(s)$ is revealed as crucial as it intends to discard (if possible) a final shape prone to exhibit instabilities.

4.5 The minimisation problem within the regularised methodology

In the proposed incrementally regularised approach, the equilibrium equations in (4) are replaced with their incrementally regularised counterparts, written as

$$\begin{aligned} \mathrm{DIV}\boldsymbol{P}_{n+1} - \lambda_{n+1}\boldsymbol{f}_0 = \boldsymbol{0}; &\qquad \text{in } \Omega_0; \\ \boldsymbol{P}_{n+1}\boldsymbol{N} = \lambda_{n+1}\boldsymbol{t}_0; &\qquad \text{on } \partial_t\Omega_0; \\ \boldsymbol{\phi} = \bar{\boldsymbol{\phi}}; &\qquad \text{on } \partial_{\boldsymbol{\phi}}\Omega_0, \end{aligned} \tag{44}$$

with $\boldsymbol{P}_{n+1}$ defined in (43), $\lambda_{n+1} = (n+1)/N$, with $n = \{0, 1, ..., N-1\}$. Therefore, the original minimisation problem (P_1) (14) is replaced by its regularised counterpart $(P_{1_{\mathrm{reg}}})$, defined as

$$(P_{1_{\mathrm{reg}}}) \quad \begin{cases} \min\limits_{\Omega_0 \in \mathcal{U}_{\mathrm{ad}}} \mathcal{J}\left(\Omega_0\right), \\ \text{s.t. } |\Omega_0| = V^* \\ \qquad \text{State equations (1), (44), and } (43)_a \end{cases} \tag{45}$$

The regularised augmented Lagrangian functional $\mathcal{L}_{\mathrm{reg}}$ is defined as

$$\begin{aligned} \mathcal{L}_{\mathrm{reg}}\left(\Omega_0, \boldsymbol{\mathcal{U}}, \boldsymbol{\mathcal{P}}, \ell_1\right) &= \mathcal{J}\left(\Omega_0, \boldsymbol{u}_N\right) \\ &\quad + \sum_{n=0}^{N-1} \mathit{\Pi}_{\mathrm{reg}}\left(\Omega_0, \boldsymbol{u}_{n+1}, \boldsymbol{p}_{n+1}\right) \\ &\quad + \ell_1\left(|\Omega_0| - V^*\right) + \frac{\gamma_1}{2}\left(|\Omega_0| - V^*\right)^2; \\ \mathit{\Pi}_{\mathrm{reg}}\left(\Omega_0, \boldsymbol{u}_{n+1}, \boldsymbol{p}_{n+1}\right) &= -\int_{\Omega_0} \boldsymbol{P}_{n+1} : \boldsymbol{\nabla}_0 \boldsymbol{p}_{n+1}\, dV \\ &\quad + \lambda_{n+1}\left(\int_{\Omega_0} \boldsymbol{p}_{n+1} \cdot \boldsymbol{f}_0\, dV \right. \\ &\quad \left. + \int_{\partial_t\Omega_0} \boldsymbol{p}_{n+1} \cdot \boldsymbol{t}_0\, dA\right), \end{aligned} \tag{46}$$

where $\boldsymbol{\mathcal{U}} = \{\boldsymbol{u}_1, ..., \boldsymbol{u}_{n+1}, ..., \boldsymbol{u}_N\}$ represent the set of solutions of the regularised equilibrium constraint (44) and $\boldsymbol{\mathcal{P}} = \{\boldsymbol{p}_1, ..., \boldsymbol{p}_{n+1}, ..., \boldsymbol{p}_N\}$, the set of adjoint state counterparts. Introduction of the expression for $\boldsymbol{P}|_{n+1}$ (43) into (46) enables to re-express $\mathit{\Pi}_{\mathrm{reg}}$ as

$$\begin{aligned} &\mathit{\Pi}_{\mathrm{reg}}\left(\Omega_0, \boldsymbol{u}_{n+1}, \boldsymbol{p}_{n+1}\right) = \\ &-\int_{\Omega_0} \boldsymbol{\nabla}_0 \boldsymbol{p}_{n+1} : g(s|_n)\, \boldsymbol{\mathcal{C}}_{\mathrm{reg}}|_n : \boldsymbol{\nabla}_0 \boldsymbol{\Delta u}_{n+1}\, dV \\ &+ \lambda_{n+1}\left(\int_{\Omega_0} \boldsymbol{p}_{n+1} \cdot \boldsymbol{f}_0\, dV + \int_{\partial_t\Omega_0} \boldsymbol{p}_{n+1} \cdot \boldsymbol{t}_0\, dA\right) \\ &-\int_{\Omega_0} \boldsymbol{\nabla}_0 \boldsymbol{p}_{n+1} : g(s|_n)\, \boldsymbol{P}|_n\, dV. \end{aligned} \tag{47}$$

The stationary condition of $\mathcal{L}_{\mathrm{reg}}$ (46) with respect to $\delta\boldsymbol{p}_{n+1} \in H_0^1(\Omega_0; \mathbb{R}^3)$ yields

$$\begin{aligned} &D\mathcal{L}_{\mathrm{reg}}[\delta\boldsymbol{p}_{n+1}] = \\ &-\int_{\Omega_0} \boldsymbol{\nabla}_0 \delta\boldsymbol{p}_{n+1} : g(s|_n)\, \boldsymbol{\mathcal{C}}_{\mathrm{reg}}|_n : \boldsymbol{\nabla}_0 \boldsymbol{\Delta u}_{n+1}\, dV \\ &+ \lambda_{n+1}\left(\int_{\Omega_0} \delta\boldsymbol{p}_{n+1} \cdot \boldsymbol{f}_0\, dV + \int_{\partial_t\Omega_0} \delta\boldsymbol{p}_{n+1} \cdot \boldsymbol{t}_0\, dA\right) \\ &-\int_{\Omega_0} \boldsymbol{\nabla}_0 \delta\boldsymbol{p}_{n+1} : g(s|_n)\, \boldsymbol{P}|_n\, dV = 0. \end{aligned} \tag{48}$$

From (48) it is possible to obtain the displacement field at load increment $n+1$, namely $\boldsymbol{u}_{n+1}$ (notice that (48) is linear with respect to $\boldsymbol{u}_{n+1}$). Furthermore, the stationary condition of $\mathcal{L}_{\mathrm{reg}}$ with respect to $\delta\boldsymbol{u}_{n+1} \in H_0^1(\Omega_0; \mathbb{R}^3)$ for the specific case where $n = N-1$ yields

$$\begin{aligned} D\mathcal{L}_{\mathrm{reg}}[\delta\boldsymbol{u}_N] = &-\int_{\Omega_0} \boldsymbol{\nabla}_0 \boldsymbol{p}_N : g(s|_n)\, \boldsymbol{\mathcal{C}}_{\mathrm{reg}}|_n : \boldsymbol{\nabla}_0 \delta\boldsymbol{u}_N\, dV \\ &+ \int_{\Omega_0} \boldsymbol{f}_0 \cdot \delta\boldsymbol{u}_N\, dV + \int_{\partial_t\Omega_0} \boldsymbol{t}_0 \cdot \delta\boldsymbol{u}_N\, dA = 0. \end{aligned} \tag{49}$$

Equation (49) enables to obtain the adjoint state at load increment $n+1$, e.g. $\boldsymbol{p}_N$. Furthermore, the stationary condition of $\mathcal{L}_{\mathrm{Reg}}$ with respect to $\delta\boldsymbol{u}_{n+1} \in H_0^1(\Omega_0; \mathbb{R}^3)$ for the case when $n \neq N-1$ yields

$$\begin{aligned} D\mathcal{L}_{\mathrm{reg}}[\delta\boldsymbol{u}_{n+1}] = &-\int_{\Omega_0} \boldsymbol{\nabla}_0 \boldsymbol{p}_N : g(s|_n)\, \boldsymbol{\mathcal{C}}_{\mathrm{reg}}|_n : \boldsymbol{\nabla}_0 \delta\boldsymbol{u}_N\, dV \\ &= 0, \end{aligned} \tag{50}$$

which yields the trivial solution $\boldsymbol{p}_{n+1} = \boldsymbol{0}$ if $n \neq N-1$ and the problem is well-posed. In this case, this is always the case due to the regularisation introduced into

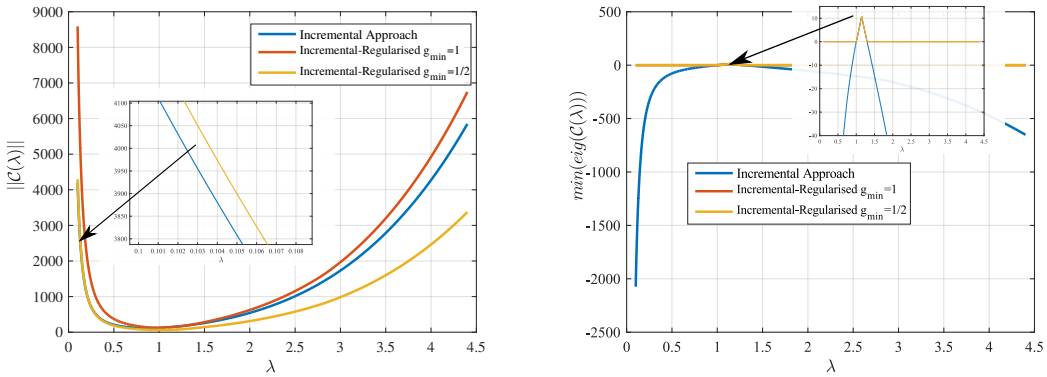

(a) (b)

Fig. 5 Behaviour of incrementally regularised approach in Section 4.4. Evolution of: (a) $||\boldsymbol{\mathcal{C}}||$; (b) minimum eigenvalue of $\boldsymbol{\mathcal{C}}$ (the minimum eigenvalue corresponding to the regularised approaches is always positive or zero).

the problem which now reveals crucial for the solution of the adjoint problem. Solution of (48) enables to obtain the displacement field at load increment $n+1$, i.e. $\boldsymbol{u}_{n+1}$. Comparison between (48) and (49) enables to identify that the last term on the right hand-side of equation (48) is the only difference between both equations. Therefore, this term accounts for the fact that $(P_{1_{\text{reg}}})$ (45) is not self-adjoint, i.e. $\boldsymbol{u}_N \neq \boldsymbol{p}_N$. Finally, the expression of the counterpart of the shape derivative in (22) for the incrementally regularised Lagrangian $\mathcal{L}_{\text{reg}}$ (46) adopts the following expression

$$\begin{aligned} D\mathcal{L}[\boldsymbol{\vartheta}] &= \int_{\partial_o\Omega_0} \vartheta_N v \, dA; \\ v &= g\left(s|_n\right)\left(\boldsymbol{P}|_n + \boldsymbol{\mathcal{C}}_{\text{reg}}|_n : \boldsymbol{\nabla}_0 \Delta\boldsymbol{u}_{n+1}\right), \end{aligned} \tag{51}$$

where use of $\boldsymbol{p}_{n+1} = \boldsymbol{0}$ (if $n \neq N-1$) has been made of in (51) (see (50)).

Remark 7. *With regards to the strategy followed to fulfil the volume constraint* (13)*, the Lagrange multiplier ℓ_1 is updated at each TO iteration $k+1$ according to $\ell_1^{k+1} = \ell_1^k + \gamma_1\left(|\Omega_0| - V^*\right)$. Furthermore, the penalty parameter is updated after every five TO iterations, multiplying its previous value by 1.2.*

□

Remark 8. *An appealing ingredient of the proposed methodology is the solution of the equilibrium equations in a consistent incrementally linearised fashion. This yields a series of incremental linear problems where the incremental displacement field is obtained without resorting to an iterative strategy (e.g non-modified Newton-Raphson). From the computational standpoint, this technique (in conjunction with the stabilisation proposed in Section 4.3) circumvents the numerical difficulties inherent to a (non-modified) Newton-Raphson scheme. However, this incremental approach entails that the equilibrium equations are not solved exactly, but approximately, due to the regularisation introduced. Therefore, the accuracy of this approach rests on a careful choice of the number of load increments and a well-defined degradation function in order to control the amount of stabilisation introduced by the regularisation parameter. In the numerical examples to follow, we will analyse the accuracy of this approach and demonstrate its impressive range of validity.*

□

4.6 Computational Strategies

In this section, we summarise the computational strategies followed by the authors in order to perform topology optimisation at large strains by means of the level-set method.

4.6.1 Strategy I: Newton-Raphson/arc-length

This strategy corresponds to the classical approach used in topology optimisation. At each TO iteration, a Newton-Raphson method can be used in order to solve the equilibrium equation (4) in an incremental fashion until convergence problems are observed. At this instant, an arc-length technique can be used in order to capture the post-buckling response of the structure until the design load is reached ($\lambda = 1$). Therefore, the TO algorithm must rely on the Lagrangian functional $\mathcal{L}$ in (16).

However, as illustrated in Figures 3 and 14, the post-buckling response of intermediate TO iterations can potentially be extremely complex and, in fact, it could be impossible to find an equilibrium configuration for the design load (Figures 3 and 13 show examples where it would be impossible to find the value of the compliance at $\lambda = 1$).

4.6.2 Strategy II: Continuation method

In order to circumvent the shortcoming associated with Strategy I, we propose a continuation method which combines the latter with the proposed technique described throughout Sections 4.1-4.5. In order to better explain this, let us assume that at a given TO iteration, a critical point has been detected by means of Strategy I at $\lambda = \lambda_{cr}$ [5]. From λ_{cr} to $\lambda = 1$, the load is then applied in a number of increments N_{post} in order to obtain a fictitious regularised post-buckling response by means of the regularisation technique proposed in Sections 4.1-4.5. Crucially, the degradation function $g(s)$ in (42) is introduced with the aim of penalising the compliance of excessively stabilised intermediate designs. Consequently, the Lagrangian functional associated with the pre-buckling region is that in (16), whereas in the post-buckling region, the Lagrangian functional corresponds to the regularised counterpart in (46).

4.6.3 Strategy III: Regularised approach

With the aim of reducing the computation burden and taking inspiration from Strategy II, we put forward a third strategy where the Newton-Raphson method of the pre-buckling stage is now circumvented. In this new strategy, at every TO iteration, the regularised approach described throughout Sections 4.1-4.5 is applied incrementally using N load increments from $\lambda = 0$ to $\lambda = 1$. Therefore, both pre- and post-buckling regions are approximated by means of the proposed method in Sections 4.1-4.5. Clearly, avoiding the use of a Newton-Raphson/arc-length technique results in a higher computational efficiency with respect to Strategy II.

5 Numerical experiments

The objective of this section is to demonstrate the performance and applicability of the proposed incrementally regularised methodology. For every increment $n+1$, and following a standard Finite Element implementation, the out-of-balance of residual vector $\mathbf{R}_{n+1}$ is computed as $\mathbf{R}_{n+1} = \mathbf{T}_n - \lambda_{n+1}\mathbf{F}_0$, where $\mathbf{F}_0$ represents the equivalent (nominal) external nodal force vector, λ_{n+1} is the load factor and $\mathbf{T}_n$ is the equivalent vector of internal forces at increment n. The unknown incremental displacement vector $\mathbf{U}$ is computed after solution of the discrete linear system $\mathbf{K}_n\mathbf{U} = \mathbf{R}_{n+1}$, where $\mathbf{K}_n$ is the discrete tangent operator obtained at the end of the load incement n. Assembly of $\mathbf{K}$ and $\mathbf{R}$ is carried out following standard Finite Element methodology (Bonet et al (2016b)). Five challenging numerical examples have been considered with the following common characteristics:

- The constitutive model considered is that of a Mooney-Rivlin model as defined in (6).
- Q_1 bi-linear (2D applications) or tri-linear (3D applications) have been used for the Finite Element discretisation of displacements $\boldsymbol{u}$ and the adjoint state field $\boldsymbol{p}$.
- A uniform Cartesian grid characterised by the number of elements in the X, Y and Z directions, denoted as N_x, N_y and N_z, respectively, has been considered.
- The hypothesis of plane stress (refer to Appendix A) has been considered for all 2D examples.
- The parameter s_{cr} of the degradation function $g(s)$ (42) is $s_{cr} = 0.1$.
- The ratio of the material parameters for void and solid regions for analysis is $\varepsilon = 10^{-5}$. In order to check the performance of the final designs, we have employed $\varepsilon = 10^{-12}$.

Finally, it is important to emphasise that all the final designs obtained have been tested at a postprocessing stage using the exact nonlinear equilibrium equations, without adding any source of artificial stiffness. Specifically, equilibrium paths have been obtained using an arc-length Newton-Raphson method in conjunction with a ratio of the material parameters for void and solid regions of 10^{-12}.

5.1 Numerical example 1

The objective of this example is two-fold:

- **OI.1.** To benchmark our in-house level-set based TO algorithm for small deformations against available results in the literature for a classical benchmark example.
- **OI.2.** To illustrate the dramatic changes with regards to the topology and the structural behaviour of the optimum structure between the linear (small deformations) and nonlinear regimes (large deformations) for problems which do not pose a challenge for the application of Strategy I.

The geometry and boundary conditions for this example are illustrated in Figure 6a. The initial seed or initial design considered is depicted in Figure 6b. The relevant material properties and simulation parameters for this specific example can be found in Table 1.

[5] λ_{cr} can be approximated by the point in the equilibrium path where λ decreases

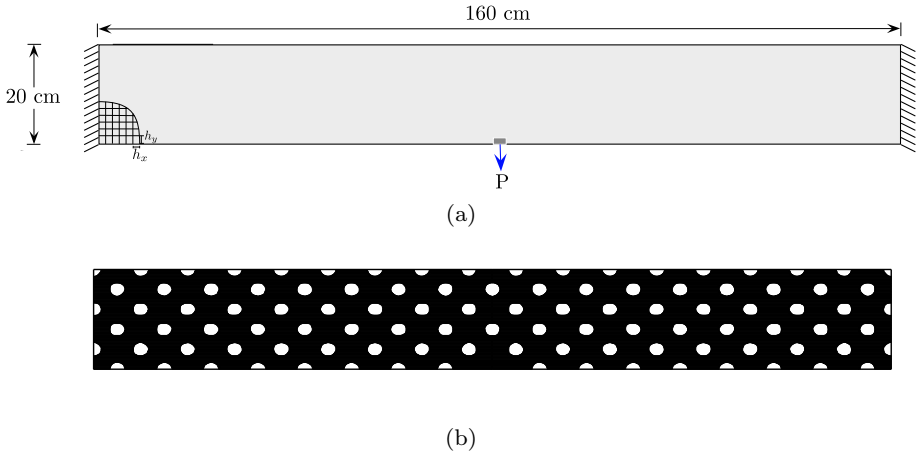

Fig. 6 Numerical example 1: (a) geometry and boundary conditions and (b) initial (non-optimum) seed.

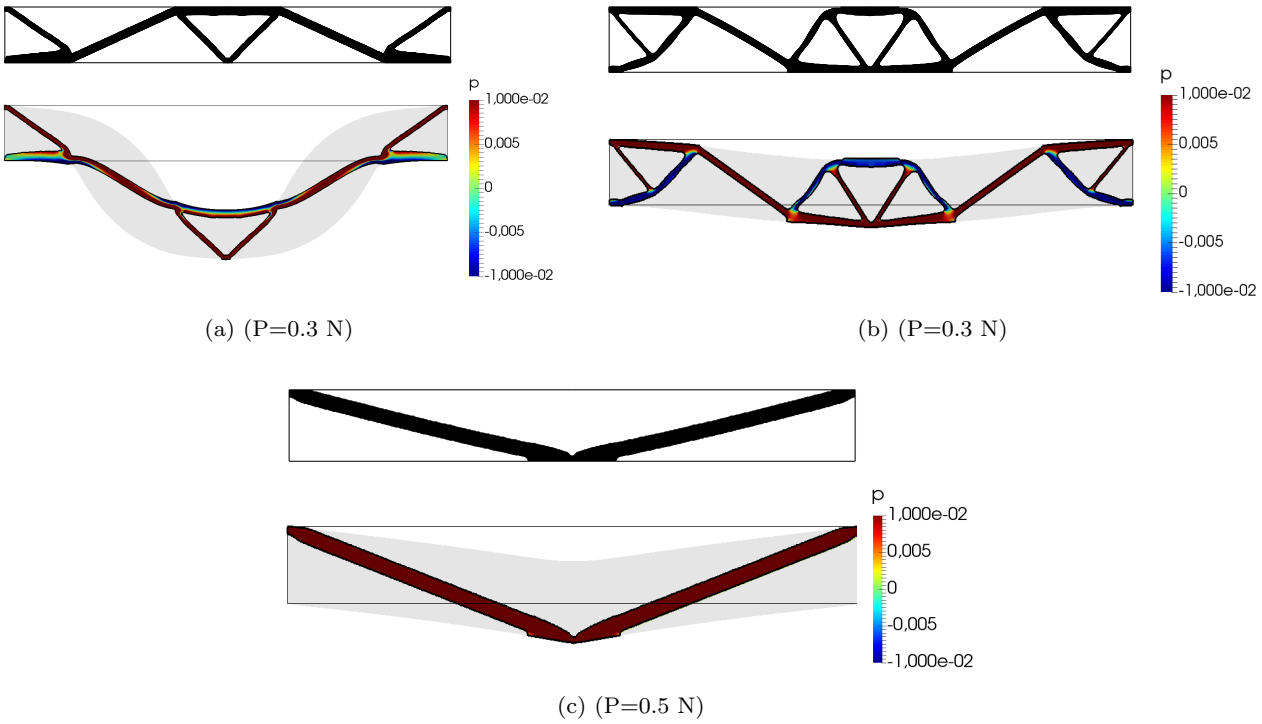

Fig. 7 Numerical example 1: Optimum design corresponding to: (a) $P = 0.3\,N$ (design obtained by means of linear solver); (b) $P = 0.3\,N$ (design obtained by means of Strategy I); (c) $P = 0.5\,N$ (design obtained by means of Strategy I). The deformed configuration and hydrostatic pressure contour plot have been obtained at a postprocessing stage through an arc-length method with $\varepsilon = 10^{-12}$.

With regards to objective **OI.1**, Figure 7a shows the final topology (initial in black and deformed in colour) configurations obtained under the unrealistic assumption of small deformations (linear solver). The colour contour represents the hydrostatic pressure p[6]. It can be observed that this topology agrees well with that in (Jung and Gea, 2004). Figure 8 provides very insightful information with regards to objective **OI.2**. Specifically, Figure 8a shows that the final design (obtained under the assumption of small deformations) is extremely compromised and exhibits a limit point for a value of P smaller than the design value of $P = 0.3\,N$. Furthermore, its equilibrium path showcases perfectly one of the plausible difficulties associated with the arc-length technique described in Section 4.1, namely, the fact that it is sometimes impossible to obtain a configuration in equilibrium with the external applied nodal force P for some topological designs.

[6] The hydrostatic pressure is obtained as $p = \frac{1}{3}\text{tr}\boldsymbol{\sigma}$ where $\boldsymbol{\sigma}$ is the Cauchy stress tensor defined as $\boldsymbol{\sigma} = J^{-1}\boldsymbol{P}\boldsymbol{F}^T$ in 3D problems and $\boldsymbol{\sigma} = (\lambda_{33}J_{2D})^{-1}\boldsymbol{P}\boldsymbol{F}^T$ for 2D problems.

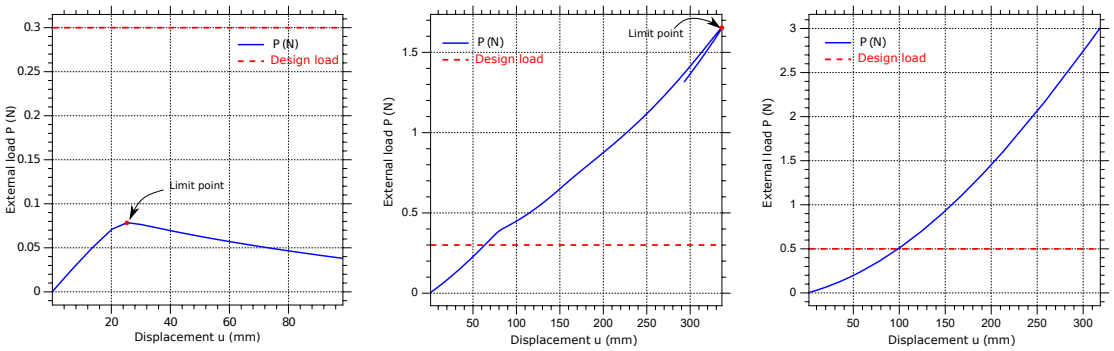

(a) (P=0.3 N) (b) (P=0.3 N) (c) (P=0.5 N)

Fig. 8 Numerical example 1: equilibrium path obtained at a postprocessing stage by means of an arc-length method and $\varepsilon = 10^{-12}$ for the three different topologies in Figure 7, corresponding to: (a) $P = 0.3\,N$ (design obtained with small strains assumption); (b) $P = 0.3\,N$ with design obtained by means of Newton-Raphson (Strategy I); (c) $P = 0.5\,N$ with design obtained by means of Newton-Raphson (Strategy I).

Table 1 Numerical example 1. Material properties (see (7)), material parameters in (6) and simulation parameters.

Material Properties	$E\|_0$	30	MPa
	$\nu\|_0$	0.3	
Material Parameters	μ_1	11.5385	MPa
	μ_2	0	MPa
	λ	17.3077	MPa
Simulation Parameters	N_x	256	
	N_y	64	
	V^*	$0.2 \cdot V_0$	

On the other hand, the design obtained using the realistic large deformations assumption (see Figures 7b and 8b), obtained with the Newton-Raphson method (Strategy I), exhibits a limit point for a value of the critical load much larger than the design load $P = 0.3\,N$ (refer to Figures 7b and 8b). This same method is now exploited for the case of a larger design load $P = 0.5\,N$. Referring to Figures 7c and 8c, it can be observed that the design for $P = 0.5\,N$ leads to a dramatically different topology. Such extreme topology yields an equilibrium path exempt from limit points (see Figure 8c).

In this example, the specific boundary conditions (both Dirichlet and Neumann) of the problem facilitate the development of a topological structure without extreme numerical difficulties, where a standard Newton-Raphson method (Strategy I) can be used to successfully converge to a final design. However, in the following examples, we will observe that other combinations of Dirichlet and Neumann boundary conditions can lead to more challenging situations characterised by severe numerical difficulties due to the presence of extensive compressive regions leading to local and/or global instabilities. In these scenarios, the classical Newton-Raphson method requires to be enhanced via the arc-length technique or, in extremely adverse (but common) situations, by means of Strategy II (and III).

5.2 Numerical example 2

The objective of this example is:

- **OII.1.** To illustrate the numerical difficulties introduced by the nucleation process triggered by the initialisation of the level-set method from a generic seed and hence, the impossibility of applying Strategy I in these cases.
- **OII.2.** To show how Strategy II can help stabilising extremely compromised regions and to provide a clear visualisation of the distribution of the regularisation parameter s over the intermediate designs obtained during the nucleation process.

The geometry and boundary conditions for this example are illustrated in Figure 9a. The initial seed considered is depicted in Figure 9b. The relevant material properties, material and simulation parameters for this specific example can be found in Table 2.

Figure 10 (left column) displays the initial topological design configurations for different design loads. Figure 10 (right column) displays their respective deformed configurations and in colour the visualisation of an invariant of the deformation gradient tensor. Furthermore, the design shown in the first row is obtained with the unrealistic small deformations assumption (linear solver). In contrast, the rest of the designs are obtained by using the realistic large deformations assumption, specifically by means of Strategy II.

As expected, it can be observed from comparison between Figures 10a-10b and 10c-10d that the design obtained with the unrealistic linear solver exhibits a

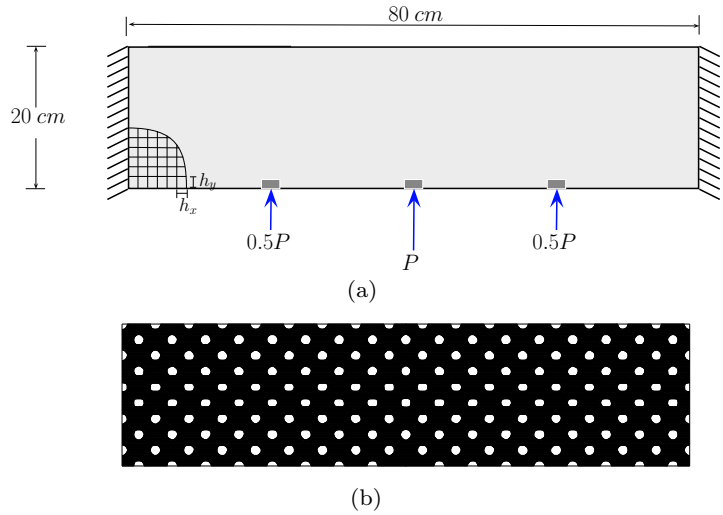

Fig. 9 Numerical example 2: (a) geometry and boundary conditions and (b) initial (non-optimum) seed.

Table 2 Numerical example 2. Material properties (see (7)), material parameters in (6) and simulation parameters.

Material Properties	$E\|_0$	0.596	MPa
	$\nu\|_0$	0.49	
Material Parameters	μ_1	0.15	MPa
	μ_2	0.05	MPa
	λ	9.7667	MPa
Simulation Parameters	N_x	256	
	N_y	64	
	V^*	$0.25 \cdot V_0$	

much larger displacement than that obtained by means of Strategy II. This implies that the compliance (objective function) is clearly more optimum in the latter case.

The designs in Figures 10c-10l have been obtained by means Strategy II, with $g_{min} = 1$ in the regularised post-buckling region of TO iterations where $\lambda_{cr} < 1$, which effectively translates into not activating the degradation function in these iterations.

Figure 11 shows the equilibrium path (obtained by means of arc-length technique and with $\varepsilon = 10^{-12}$ at a postprocessing stage, hence without any source of artificial stiffness) corresponding to the six designs in Figure 10. It can be observed that for all the designs (including that corresponding to the linear analysis in Figure 11a), the limit point (in case this exists) occurs at a load value above the design load ($\lambda_{cr} > 1$), which means that all designs are safe.

Figure 10 shows also the deformed design configurations along with the contour plot distribution of the hydrostatic pressure p. This field is an extremely useful indicator to illustrate the distribution of tensile or compressive stress within the structure. Regarding objectives **OII.1** and **OII.2**, Figure 12 shows the contour plot distribution of the regularisation parameter s (defined in equation 39) for some intermediate TO iterations where $\lambda_{cr} < 1$ and hence, where the arc-length is continued by means of the incremental regularised approach in Sections 4.1-4.5 (Strategy II). It is worth observing from this figure how the regularisation parameter s is concentrated in extremely localised regions where the buckling occurs, attaining a value of almost zero in the rest of the domain Ω_0.

From Figures 12a-12c, it is worth noticing the presence of extremely thin structural parts highly compressed as well as disconnected regions. These structural features are responsible for the numerical difficulties for the solution of the state and adjoint equations (17) and (18), respectively, posing serious limitations to the robust applicability of the arc-length technique throughout the entire equilibrium path. This can be observed in Figure 13, where the equilibrium path exhibits a complex snap-back pattern, with the arc-length eventually failing before the design load $P = 2\,N$ is attained. In addition, the effect of the regularisation in the post-buckling region, both with no degradation (i.e. $g_{min} = 1$) and with degradation (i.e. $g_{min} = 0.5$), can be observed in this Figure. In particular, both choices of g successfully stabilise the thin structural components highlighted in red in Figure 13, subjected to high compressions. Clearly, when degradation is not considered ($g_{min} = 1$), a stiffer response is observed.

5.3 Numerical example 3

The objective of this example is:

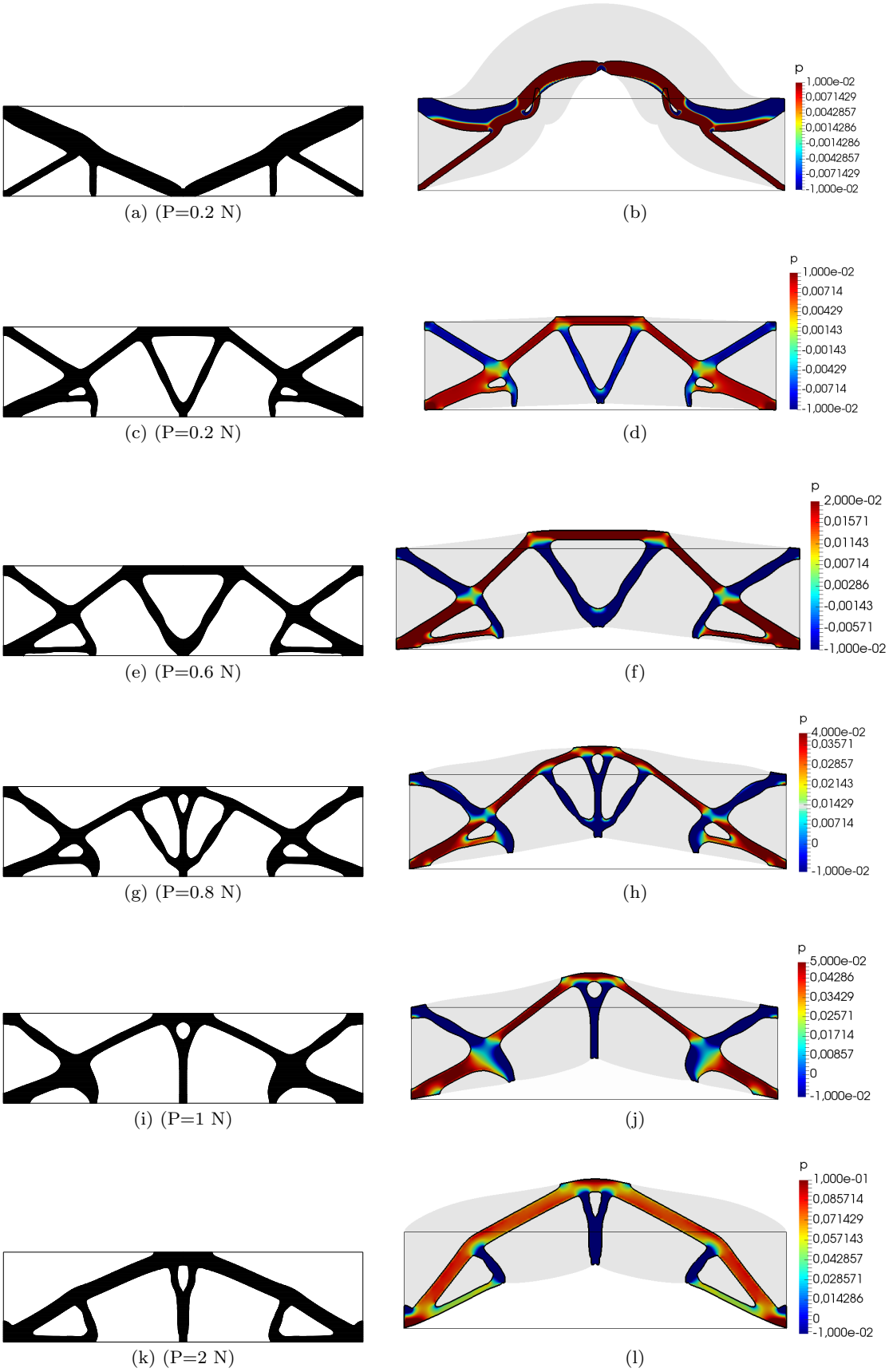

Fig. 10 Numerical example 2: optimum design (left column) for: (a) $P = 0.2\,N$ (obtained with linear solver); (c) $P = 0.2\,N$ (obtained with Strategy II); (e) $P = 0.6\,N$ (Strategy II); (g) $P = 0.8\,N$ (Strategy II); (i) $P = 1\,N$ (Strategy II); (k) $P = 2\,N$ (Strategy II). $g_{min} = 1$, $N = 10$ for the post-buckling region in Strategy II. Right column: postprocessing stage and contour plot distribution of p and deformed configuration obtained by means of arc-length and $\varepsilon = 10^{-12}$.

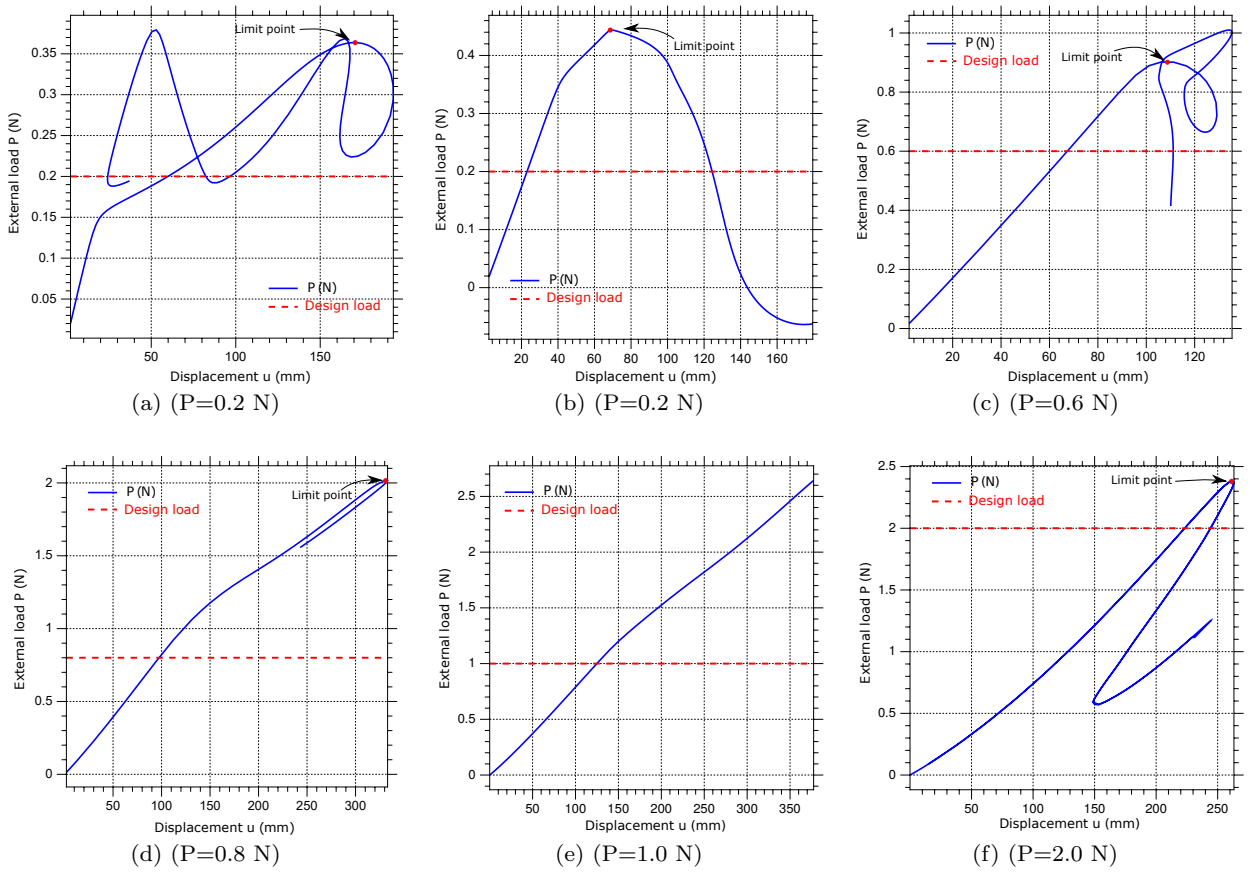

(a) (P=0.2 N) (b) (P=0.2 N) (c) (P=0.6 N)

(d) (P=0.8 N) (e) (P=1.0 N) (f) (P=2.0 N)

Fig. 11 Numerical example 2: equilibrium paths obtained by means of arc-length and $\varepsilon = 10^{-12}$ (no artificial stiffness) for the six different topologies in Figure 10 corresponding to: (a) $P = 0.2\,N$ (design obtained with linear solver); (b) $P = 0.2\,N$ (design obtained with Strategy II); (c) $P = 0.6\,N$ (Strategy II); (d) $P = 0.8\,N$ (Strategy II); (e) $P = 1\,N$ (Strategy II); (f) $P = 2\,N$ (Strategy II). $g_{min} = 1$, $N = 10$ for post-buckling regions in Strategy II.

– **OIII.1.** To check the robustness of Strategy II in a classical benchmark problem of TO at large strains.

The geometry and boundary conditions for this example are illustrated in Figure 14a. The initial seed considered is depicted in Figure 14b. The relevant material properties, material and simulation parameters for this specific example can be found in Table 3.

Table 3 Numerical example 3. Material properties (see (7)), material parameters in (6) and simulation parameters.

Material Properties	$E\|_0$	0.8736	MPa
	$\nu\|_0$	0.4559	
Material Parameters	μ_1	0.15	MPa
	μ_2	0.15	MPa
	λ	2.8034	MPa
Simulation Parameters	N_x	192	
	N_y	64	
	V^*	$0.4 \cdot V_0$	

Figures 15a, 15c and 15e display the final (deformed) topological design and equilibrium paths obtained for loads $P = 0.1\,N$, $P = 0.2\,N$ and $P = 0.4\,N$ using Strategy II.

Figure 16 illustrates perfectly Strategy II. For a given TO iteration (bottom axis), a blue bar represents the pre-buckling region of the equilibrium path whereby the arc-length method can be employed. For a large number of TO iterations, the evolving structure is stable and therefore, the bars are blue from $0 < \lambda < 1$, where λ represents the applied load factor (vertical axis). However, we observe that at certain intermediate TO iterations, the corresponding intermediate design is unstable and hence, the arc-length needs to be continued with the regularised approach described throughout Sections 4.1-4.5. From the right hand-side of Figure 16, it can be clearly appreciated that for their corresponding critical load factors, the designs are extremely compromised due to the presence of disconnected elements and localised buckling, yielding extremely complex post-buckling behaviours.

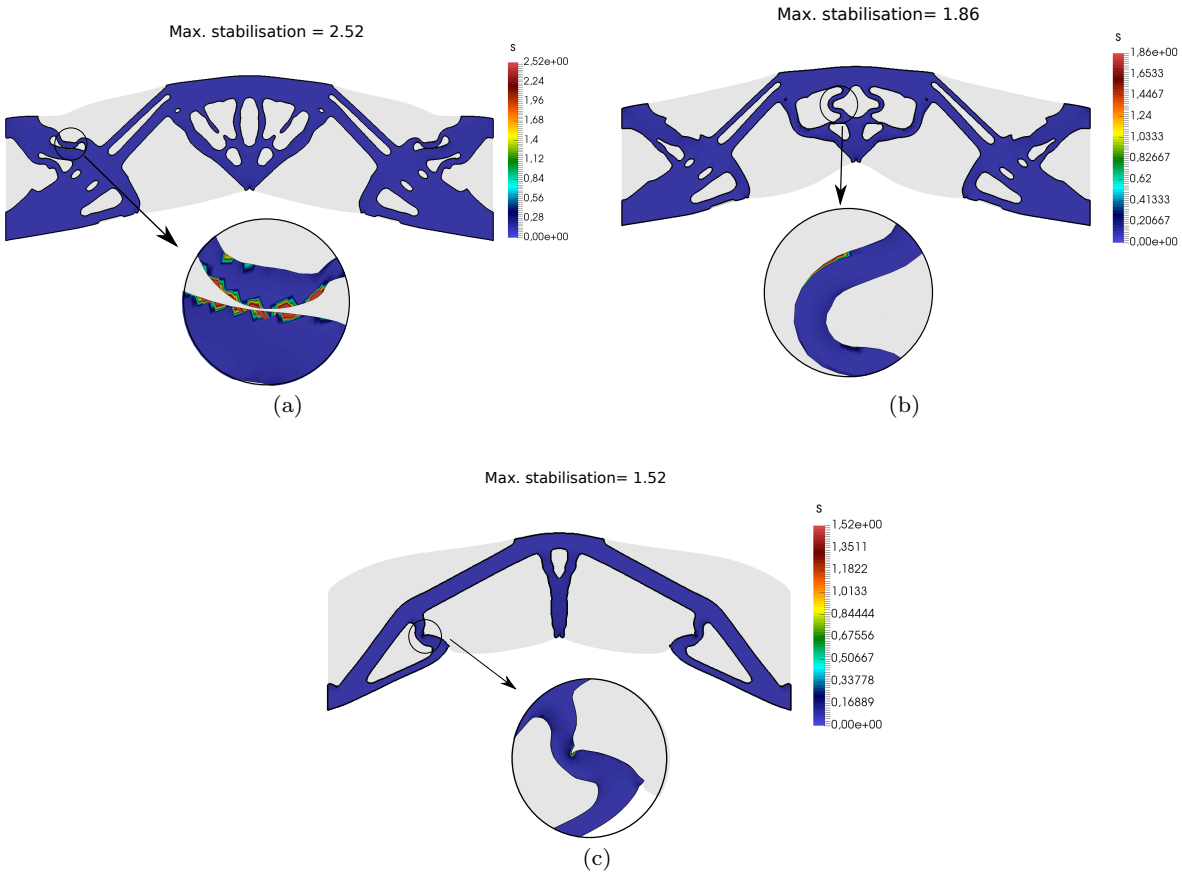

Fig. 12 Numerical experiment 2: deformed configuration and contour plot distribution of the regularisation parameter s in (39) for design load $P = 2\,N$ for the intermediate optimisation iterations (It): (a) It=32; (b) It=52; (c) It=181.

This precludes the use of Strategy I at these iterations, justifying the use of the regularisation method for the post-buckling region.

Crucially, from Figure 16 it can also be observed that instabilities do not occur in the final TO iterations. Therefore, only the arc-length is used in those final iterations, guaranteeing that the exact physics are solved (no regularisation needs to be added), hence restricting the use of the regularised approach to those TO iterations where numerical difficulties arise.

5.4 Numerical example 4

The objectives of this example are:

- **OIV.1.** To determine the applicability of the computationally efficient Strategy III and compare it against Strategy II.
- **OIV.2.** To determine the effect of the number of load increments N and the value of g_{min} (featuring in the definition of the degradation function, see equation (42)) on the accuracy of Strategy III with respect to the exact satisfaction of the equilibrium constraint.

The geometry and boundary conditions for this example are illustrated in Figure 17a. The initial seed considered is depicted in Figure 17b. The relevant material properties, material and simulation parameters for this specific example can be found in Table 4.

Objective **OIV.1** is demonstrated in Figure 18, where two different methodologies are compared: (1) Strategy II and (2) Strategy III, the latter with and without degradation function. The first two rows correspond to a design load $P = 0.05\,N$ and the last two rows correspond to a design load $P = 0.15\,N$.

In Figure 18a, topological (final configuration) designs, shown in black colour contour in the left column (a, g), are obtained using Strategy II, whereby the arc-length is continued with the proposed regularised method with $g_{min} = 1$ and $N = 30$. Like in previous example 5.3, by using Strategy II, numerical instabilities would be obtained at intermediate TO iter-

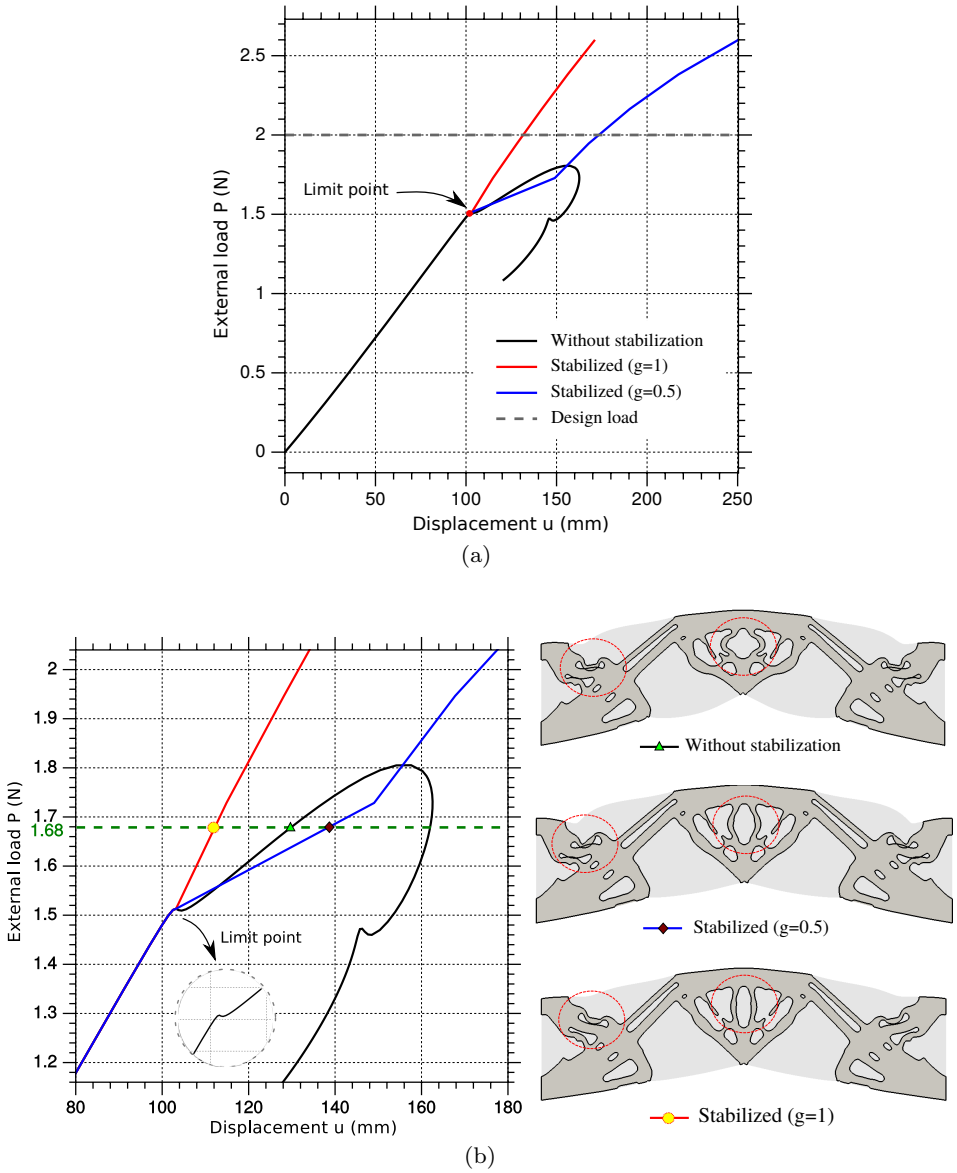

Fig. 13 Numerical example 2: (a) complex equilibrium path obtained for design load $P = 2\,N$ at intermediate optimisation iteration $It = 43$ by means of arc-length (black line) and arc-length+regularised behaviour (Strategy II) for both $g_{min} = 1$ (red line) and $g_{min} = 0.5$ (blue line); (b) zoom near the post-instability region and deformed configurations associated with the three techniques aforementioned.

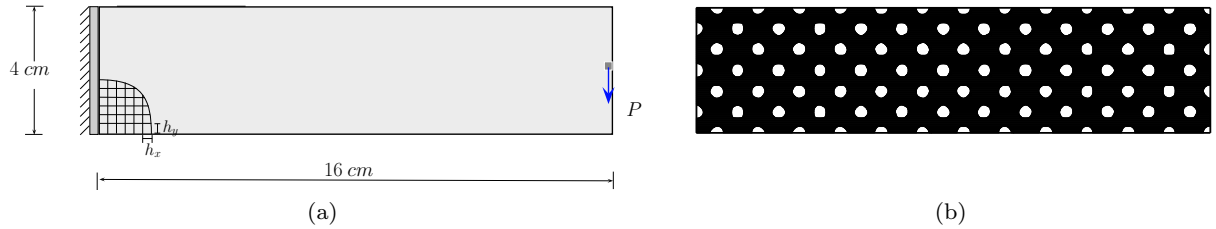

Fig. 14 Numerical example 3: (a) geometry and boundary conditions and (b) initial (non-optimum) seed.

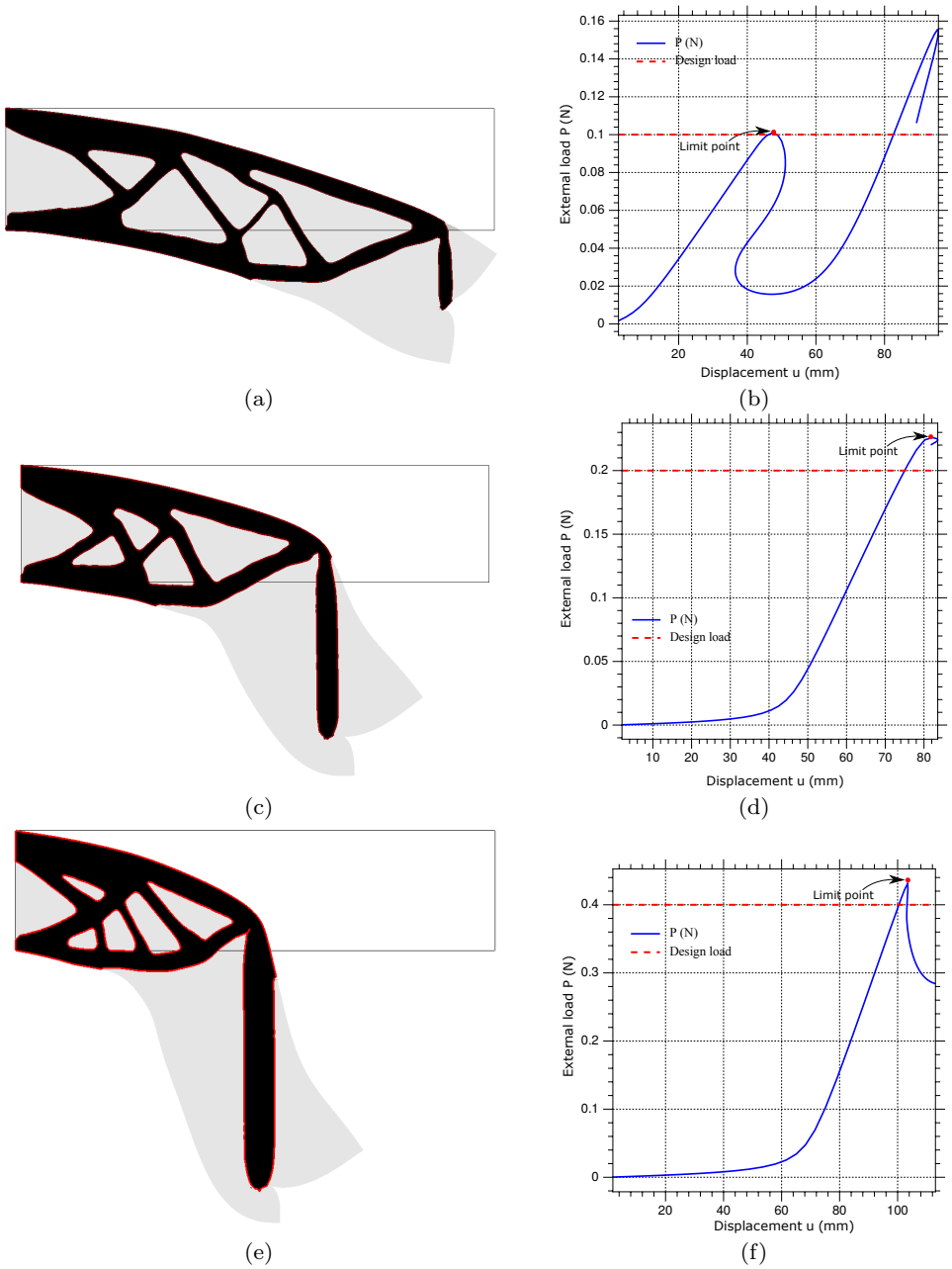

Fig. 15 Numerical example 3: optimum design and deformed configuration (left column) for: (a) $P = 0.1\,N$; (c) $P = 0.2\,N$; (e) $P = 0.4\,N$. The three designs have been obtained by means of Strategy II ($g_{min} = 1, N = 30$). Right column: postprocessing stage and equilibrium path obtained by means of arc-length and $\varepsilon = 10^{-12}$.

ations, forcing the continuation of the arc-length with the regularised approach (a similar behaviour as that depicted in Figure 16 is in fact obtained). These instabilities eventually vanish, yielding a stable design in the final TO iterations.

The centre column of Figure 18 displays topological (final configuration) designs, shown in black colour contour (b, h), obtained using Strategy III all load increments (with $g_{min} = 1$). Finally, the right column displays topological (final configuration) designs, shown in black contour in the right column (c, i), obtained using Strategy III for all load increments (with $g_{min} = 1/3$).

Let us recall that when using Strategy III, the regularised approach is applied for the entire design loading at every TO iteration. In this strategy, the number of load increments N is crucial in order to yield a sufficiently accurate response based on this linearised and stabilised approximation. For instance, if the equilibrium path associated with a design experiences a softening at a value of the accumulated factor close to the

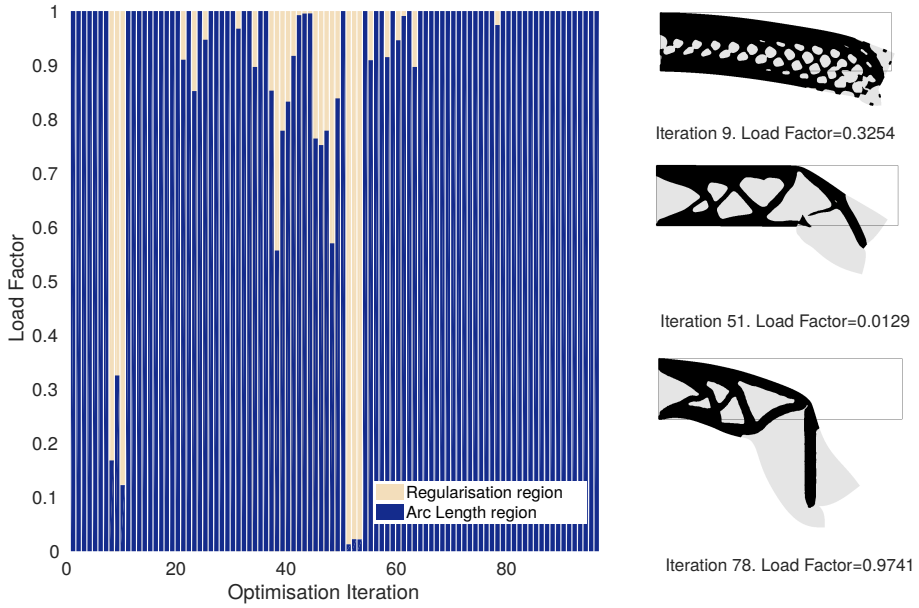

Fig. 16 Numerical experiment 3: Diagrammatic representation of Strategy II. For a given TO iteration (bottom axis), a blue bar represents the pre-buckling region of the equilibrium path whereby the arc-length method has been employed. A grey bar represents the post-buckling region (if it exists) whereby, at a critical load factor (vertical axis), we switch from the arc-length technique to the regularised approach in Sections 4.1-4.5. A value of 1 for the load factor represents the design load. On the right hand side we observe extremely compromised intermediate designs at their corresponding critical load factors for TO iterations 9, 51 and 78, where the arc-length needs to be continued with the regularisation approach.

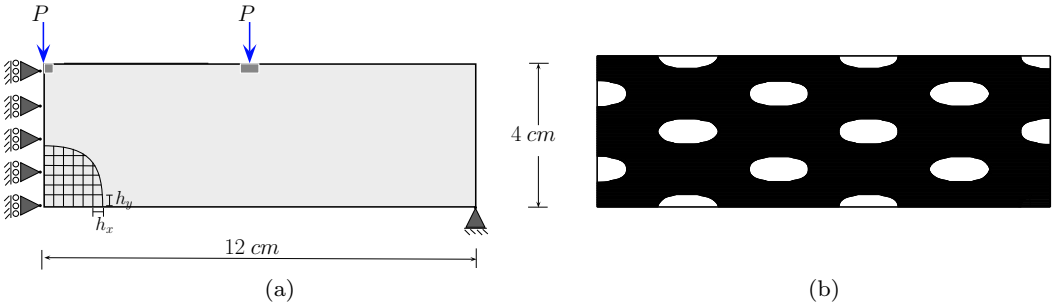

Fig. 17 Numerical example 4: (a) geometry and boundary conditions and (b) initial (non-optimum) seed.

Table 4 Numerical example 4. Material properties (see (7)), material parameters in (6) and simulation parameters.

Material Properties	$E\|_0$	0.8736	MPa
	$\nu\|_0$	0.4559	
Material Parameters	μ_1	0.15	MPa
	μ_2	0.15	MPa
	λ	2.8034	MPa
Simulation Parameters	N_x	192	
	N_y	64	
	V^*	$0.4 \cdot V_0$	

design load i.e. $\lambda \approx 0.85$, since we might be left with few load increments in order to reach $\lambda = 1$, the resulting approximation could translate effectively in a overestimation of the response of the structure (see for instance Figures 18b, 18h and 19a, where the red line corresponds to the real deformation predicted by an arc-length method whereas the black contour represents the deformation predicted by means of Strategy III). The use of the function $g(s)$ helps preventing this shortcoming associated with Strategy III (see Figures 18c, 18i and 19b). This is a consequence therefore of the fact that with Strategy III, a good approximation of the physics is intrinsically related to the choice of a sufficiently large number of load increments N, which is a priori unknown. Nevertheless, we explore this strategy in this example because of its benefits from the computational efficiency standpoint.

In Figure 18, for the smaller design load $P = 0.05\,N$, left and centre approaches (Strategy II and Strategy III with $g_{min} = 1$) give almost identical results and the

differences between the black contour and the red line are almost undistinguishable. In this case, no degradation function has been activated (i.e. $g_{min} = 1$), which, as already discussed, can potentially incur in a (possibly) undesired overestimation of the structural stiffness when using Strategy III. This detrimental feature can be clearly appreciated in Figures 18h and 19a, corresponding to design loads $P = 0.15\,N$ and $P = 0.3\,N$. The objective of the degradation function g (introduced in (40)) is precisely to circumvent this drawback. We can clearly see from Figures 18c, 18i and 19b that when using Strategy III with $g_{min} = 1/3$, the predicted deformation (black contour) underestimates the exact deformation (highlighted in red). Notice that although the stabilisation yields a higher structural stiffness than the exact structural response (see Figures 18h and 19a), the degradation function is responsible for the in general, softer (but stable) response with respect to the latter.

An interesting aspect that must be stressed, already indicated in Section 5.1, is the fact that topological changes in the nonlinear regime tend to minimise the existence of areas subjected to compressions whilst maximising those subjected to tractions (for overall structural stability). See for instance Figure 20. In this example, the specific choice of boundary conditions make it impossible to completely eliminate the areas subjected to compression (as opposed to the numerical example in Section 5.1). Unavoidably, two (compressed) bars must remain in the final design in order to transfer the applied nodal forces to the horizontal (tensioned) bar. Therefore, it is the boundary conditions that dictate the complexity and the challenging nature associated with the solution of the state equation.

Furthermore, Figure 21 shows the contour plot distribution of the regularisation parameter s defined in (39) for some intermediate optimisation iterations (It). Let us recall that this parameter informs about the loss of positive definiteness of the elasticity tensor. Notice that 21a-b correspond to TO iterations 13 and 23. The maximum value attained in these figures by the regularisation parameter is considerably large ($s_{max} = 27.1$ and $s_{max} = 2.13$, respectively) and is extremely localised in the regions where instabilities would develop if they were not stabilised. However, in Figure 21c, the value of the regularisation parameter (extremely concentrated in the area where the nodal loads are applied) is much smaller, i.e. $s_{max} = 0.67$. It is important to clarify that even though s is not completely zero everywhere for Figure 21c, this figure corresponds to a stable design, namely, its critical load is larger than the design load (see the associated arc-length in Figure 19d). This clearly showcases that local positive definiteness of the elasticity tensor is a sufficient but not necessary condition to guarantee global stability. In other words, the instability does not develop immediately after the elasticity tensor loses positive definiteness locally, although when the structure becomes unstable, then the maximum value of s increases considerably with respect to pre-buckling stages.

Finally, within Strategy III we examine the effect of the number of load increments N and the value of g_{min} in the correct satisfaction of the exact physics of the problem (objective **OVI.3**). For the design obtained in Figure 19, we see from Figure 22 that for $g_{min} = 1$, the value of the predicted compliance tends to that predicted by the arc-length method (exact solution, see dashed line in Figure 22) as N increases. For low values of N, it is clear that the predicted compliance is slightly smaller than the exact solution. On the contrary, we can see from this figure that introducing penalisation ($g_{min} = 1/2$ and $g_{min} = 1/3$), a softer response is obtained.

5.5 Numerical example 5

The objective of this example is:

– **OV.1.** To demonstrate the applicability of the proposed incrementally regularised approach in Section 4.3 to large scale three dimensional applications.

The geometry and boundary conditions for this example are illustrated in Figure 23a. The initial seed considered is depicted in Figure 23b. The relevant material properties, material and simulation parameters for this specific example can be found in Table 5.

Table 5 Numerical example 5. Material properties (see (7)), material parameters in (6) and simulation parameters.

Material Properties	$E\|_0$	0.8736	MPa
	$\nu\|_0$	0.4559	
Material Parameters	μ_1	0.15	MPa
	μ_2	0.15	MPa
	λ	2.8034	MPa
Simulation Parameters	N_x	82	
	N_y	32	
	N_z	16	
	V^*	$0.2 \cdot V_0$	

Taking advantage of the computational efficiency of Strategy III, and bearing in mind its limitations, we apply Strategy III for the TO of this three-dimensional example. The left column of Figure 24 shows the real deformed configuration and the contour plot distribution

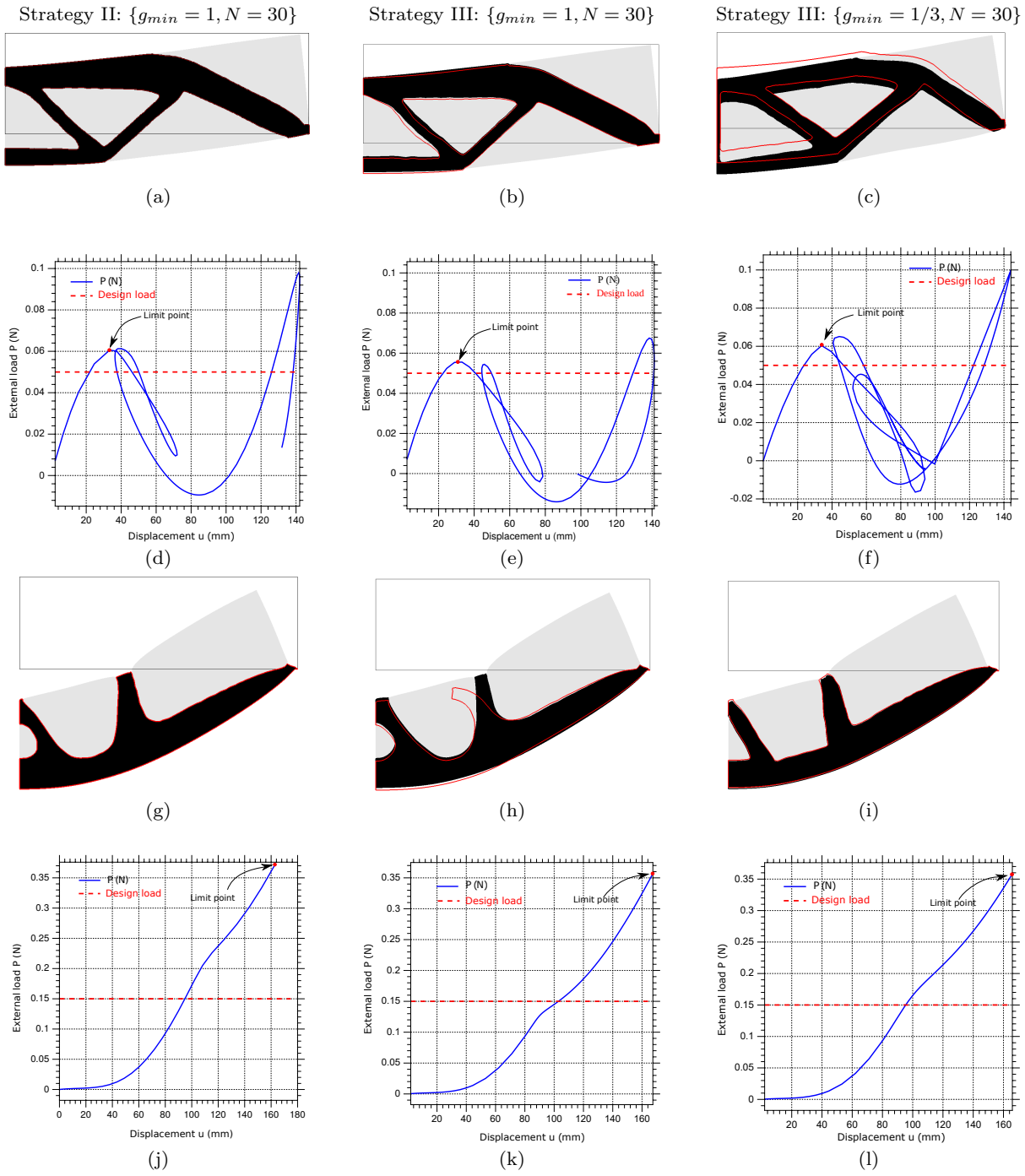

Fig. 18 Numerical example 4: final designs and associated equilibrium paths for $P = 0.05\,N$ (figures (a)-(f)) and $P = 0.15\,N$ (figures (g)-(l)) obtained by means of: (left column) Strategy II with $g_{min} = 1$ in the post-buckling region; (center column) Strategy III $g_{min} = 1$; (right column) Strategy III with $g_{min} = 1/3$. The equilibrium paths have been obtained by means of arc-length technique and $\varepsilon = 10^{-12}$ in order to avoid artificial stiffness. The red line represents the deformation obtained by means of the arc-length technique with $\varepsilon = 10^{-12}$ (without numerical stiffness).

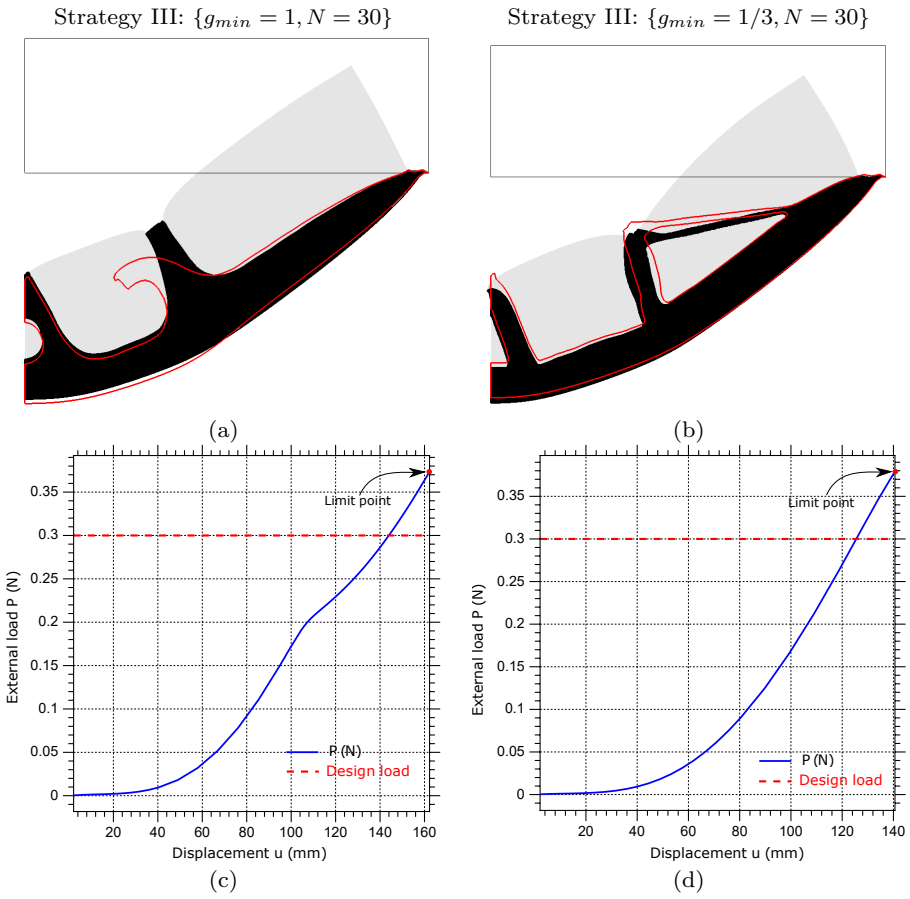

Fig. 19 Numerical example 4: final designs and associated equilibrium paths for $P = 0.3\,N$ obtained by means of: (left column) Strategy III with $g_{min} = 1$; (right column) Strategy III with $g_{min} = 1/3$. The equilibrium paths have been obtained by means of arc-length technique and $\varepsilon = 10^{-12}$ in order to avoid artificial stiffness. The red line represents the deformation obtained by means of the arc-length technique with $\varepsilon = 10^{-12}$ (without numerical stiffness).

of the hydrostatic pressure p for: (i) $P = 0.001\ N/mm^2$ using a linear solver; (ii) $P = 0.001\ N/mm^2$ using Strategy III with $g_{min} = 1/3$; (iii) $P = 0.002\ N/mm^2$ using Strategy III with $g_{min} = 1/3$. The right column of Figure 24 shows how a considerably large portion of the structure obtained by means of the linear solver (see Figure 24b) is significantly reduced when the solution is analysed with a nonlinear solver (Strategy III), in agreement with the previous numerical experiments.

6 Conclusions

The paper has introduced a novel computational approach for the topology optimisation of hyperelastic materials at large strains, still representing a challenging open problem in topology optimisation. Specifically, two computational strategies have been proposed. The first strategy (denoted as Strategy II in the paper) resorts to an arc-length in the pre-buckling region of intermediate topology optimisation iterations where numerical difficulties arise, and is then continued by a novel regularisation technique in the post-buckling region. In the second strategy (denoted as Strategy III in the paper), the regularisation technique is used for the entire loading at each topology optimisation iteration.

The regularisation technique (featuring in both computational strategies) seeks the relaxation of the optimisation Lagrangian by combining the following key features: the equilibrium equations are solved approximately in a consistently linearised incremental fashion, splitting the total design load in N (user defined) load increments. At each load increment, the elasticity tensor is regularised preventing its loss of positive definiteness, and, hence, that of the tangent operator. In order to prevent excessive regularisation (or equivalently, stabilisation), we propose the definition of a scalar indicator (at a quadrature point level) which can quantify the violation of the positive definiteness of the elasticity tensor. Based on this parameter, and inspired from the field of damage mechanics and phase-field methods to fracture, we advocate for a combined use of the regularisation approach with a penalisation function.

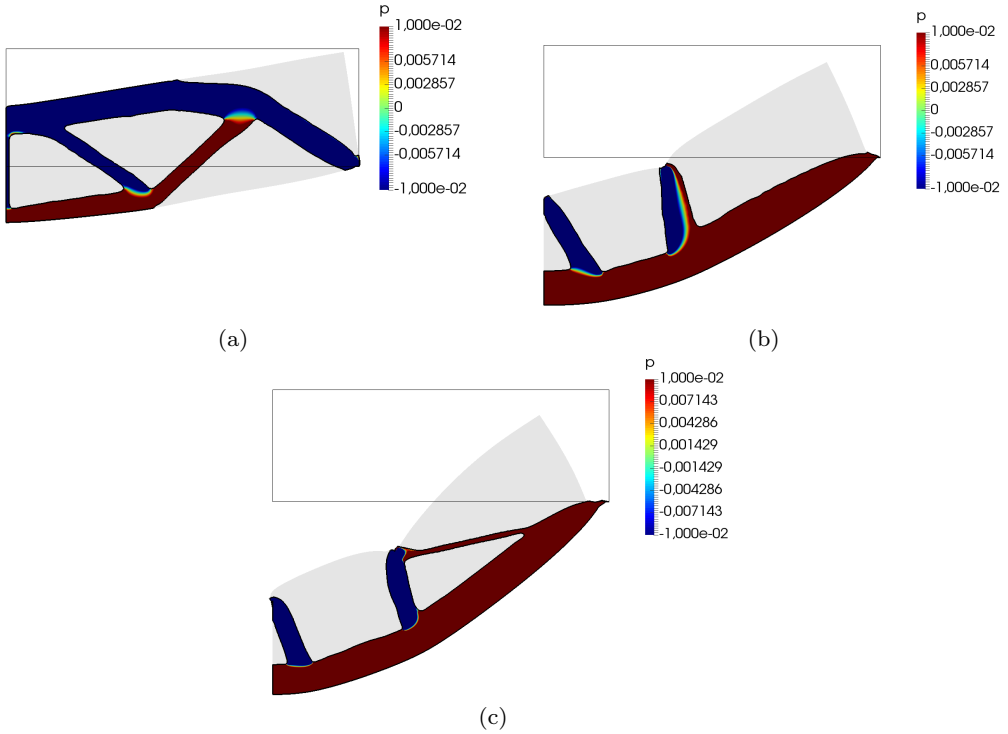

Fig. 20 Numerical example 4: final designsfor: (a) $P = 0.05\,N$; (b) $P = 0.1\,N$ and (c) $p = 0.3\,N$. Designs obtained by means Strategy III with $g_{min} = 1/3$ and $N = 30$. Deformed configuration and pressure contour plot obtained at a postprocessing stage by means of arc-length technique and $\varepsilon = 10^{-12}$ in order to avoid numerical stiffness.

Finally, a series of numerical examples have been included in order to illustrate in a comprehensive manner the robustness and applicability of the proposed methodology. Crucially, the performance of all the designs obtained in the numerical examples section has been tested at a postprocessing stage without adding any source of artificial stiffness. Specifically, an arc-length Newton-Raphson method has been employed in conjunction with a ratio of the material parameters for void and solid regions of 10^{-12}.

7 Acknowledgements

The first and third authors acknowledge the support provided by the Sêr Cymru National Research Network under the Ser Cymru II Fellowship "Virtual engineering of the new generation of biomimetic artificial muscles", funded by the European Regional Development Fund. The first author also acknowledges the support provided by Ministerio de Ciencia, Innovación y Universidades, for the award of a Juan de la Cierva Formación Fellowship. Additionally, this research was partially supported by the AEI/FEDER and UE under the contracts DPI2016-77538-R and by the Fundación Séneca (Agencia de Ciencia y Tecnología de la Región de Murcia (Spain)) under the contract 20911/PI/18.

8 Replication of Results

Regarding reproducibility of results, the following remarks apply:

- The code used to run the numerical examples in Section 5 is comprised of the following standard ingredients: (i) level-set code (Laurain, 2018); (ii) nonlinear continuum mechanics code (Bonet et al, 2016b); (iii) incrementally linearised solver (Poya et al, 2016); (iv) a bisection algorithm to determine the stabilisation required (Burden et al, 2015).
- Equilibrium paths displayed for the final designs have been obtained by means of an standard arc-length technique (Bonet et al, 2016b).
- For those readers interested in using our in-house platform, the authors are happy to be contacted.

A Particularisation to plane stress

Plane stress is suitable for many industrial applications. In this context, the three dimensional deformation gradient tensor $\boldsymbol{F}$ is expressed in terms of its in-plane component $\boldsymbol{F}_{2D}$ and the out of plane thickness stretch λ_{33} component as

$$\boldsymbol{F} = \begin{bmatrix} \boldsymbol{F}_{2D} & \boldsymbol{0}_{2\times 1} \\ \boldsymbol{0}_{1\times 2} & \lambda_{33} \end{bmatrix}. \tag{52}$$

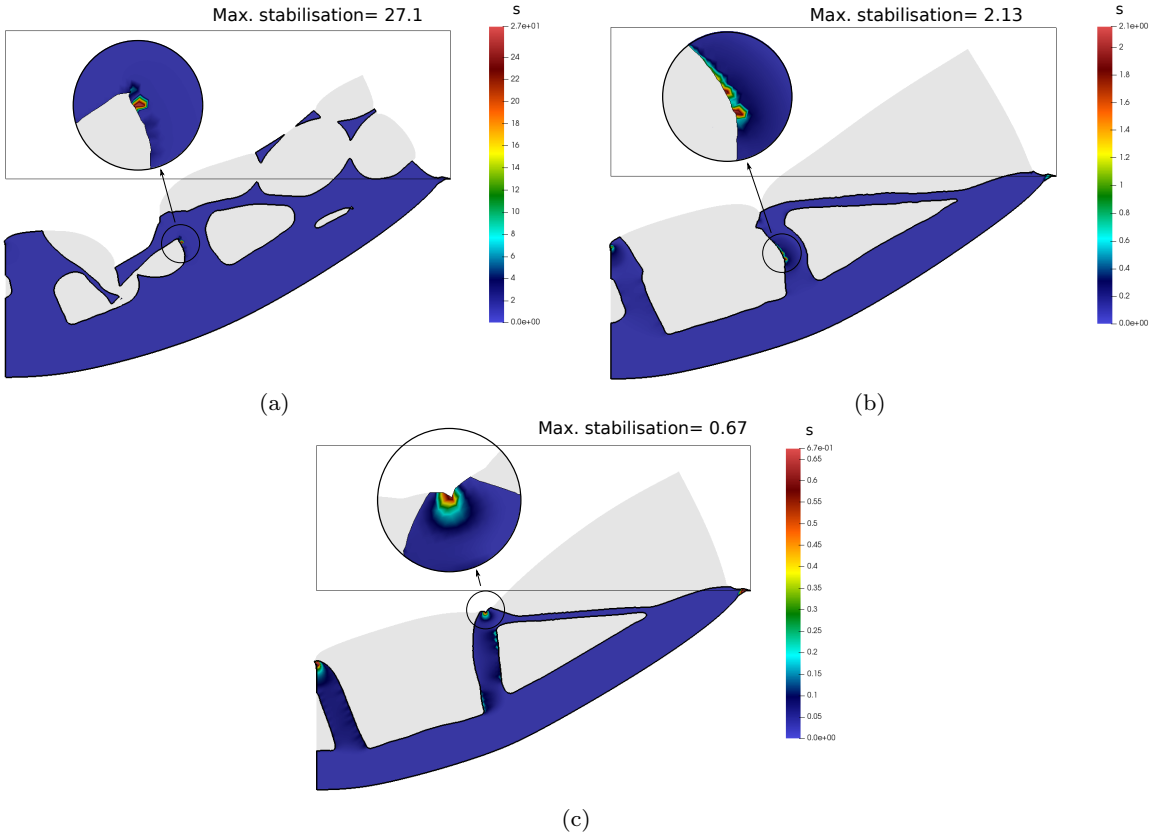

Fig. 21 Numerical experiment 4: deformed configuration and contour plot distribution of the regularisation parameter s in (39)b for design load $P = 2\,N$ for the optimisation iterations (It): (a) It=11; (b) It=13; (c) It=23. Strategy III with $g_{min} = 1/3$ and $N = 30$.

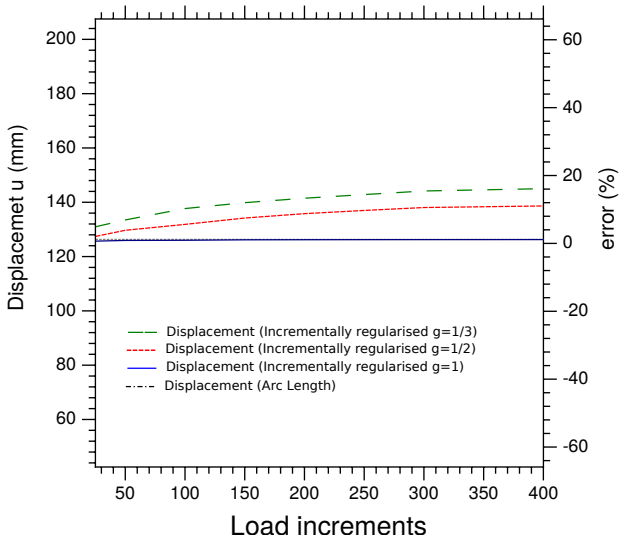

Fig. 22 Numerical example 4: Analysis at a postprocessing stage of the relative error between the real deformation (obtained by means of an arc-length technique) at the point where the load P is applied and the incrementally linearised methodology in Section 4 with an increasing value of the number of load increments N and the value of g_{min}. Analysis performed on the final design obtained for $P = 0.3\,N$ (see Figures 15(c)-(d)). For $N = 30$ (the value used in the simulations) the relative error is lower than 0.6%.

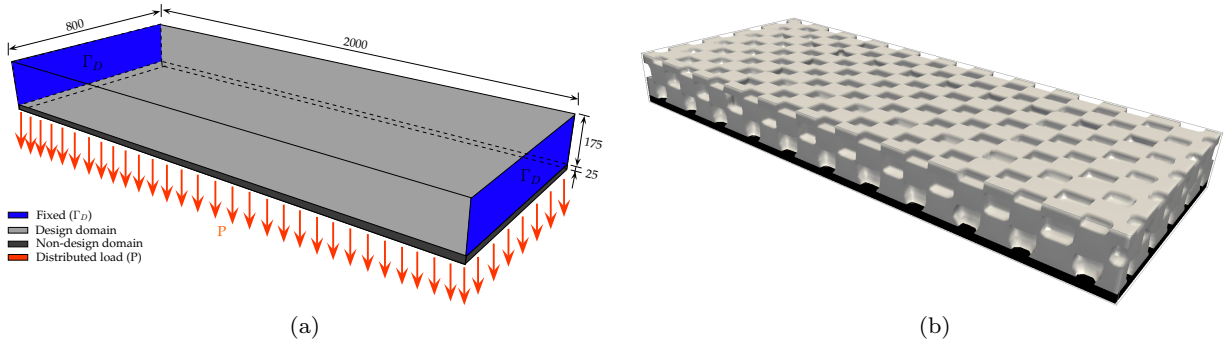

(a) (b)

Fig. 23 Numerical example 5: (a) geometry and boundary conditions and (b) initial (non-optimum) seed.

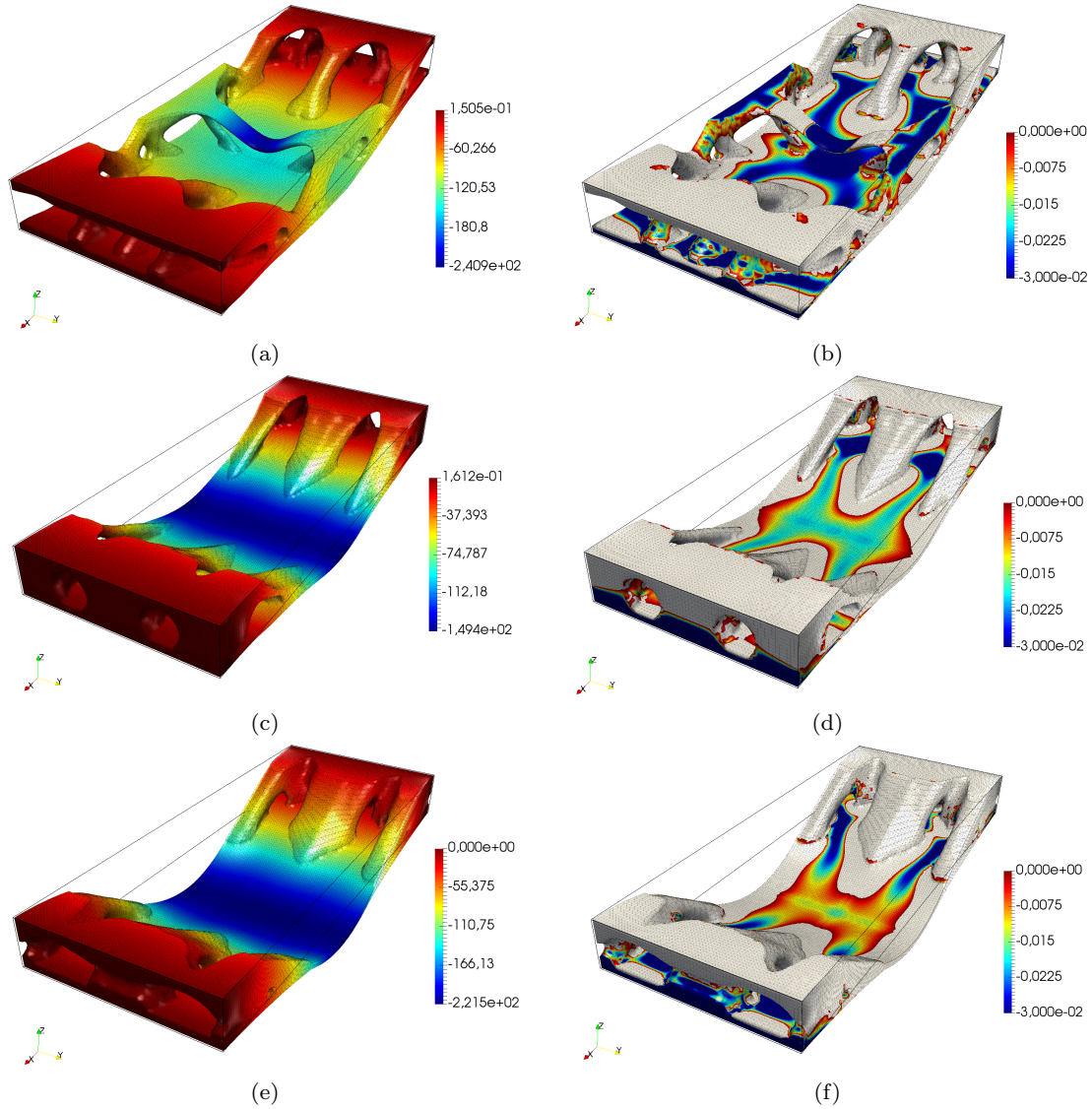

(a) (b) (c) (d) (e) (f)

Fig. 24 Numerical example 5: Contour plot distribution of p (left column) and contour plot distribution of compressions ($p \leq 0$, right column) for: (a-b) $P = 0.001\ N/mm^2$ (design obtained with linear solver); (c-d) $P = 0.001\ N/mm^2$ (design obtained with solver in Section 4: $\{g_{min} = 1/3, N = 15\}$); (e-f) $P = 0.002\ N/mm^2$ (design obtained with solver in Section 4: $\{g_{min} = 1/3, N = 15\}$). The deformed configuration and the contour plot distribution of p have been obtained by means of arc-length technique and $\varepsilon = 10^{-12}$.

Making use of (2), the Jacobian J and the co-factor $\boldsymbol{H}$ of $\boldsymbol{F}$ can be defined as

$$\begin{aligned} &J = J_{2D}\lambda_{33};\\ &\boldsymbol{H} = J\boldsymbol{F}^{-T} = \begin{bmatrix} \lambda_{33}\boldsymbol{H}_{2D} & \boldsymbol{0}_{2\times 1} \\ \boldsymbol{0}_{1\times 2} & J_{2D} \end{bmatrix}, \end{aligned} \tag{53}$$

with $\boldsymbol{H}_{2D}$ and J_{2D} defined as

$$\boldsymbol{H}_{2D} = (\boldsymbol{F}_{2D} : \boldsymbol{I})\,\boldsymbol{I} - \boldsymbol{F}_{2D}^T; \qquad J_{2D} = \frac{1}{2}\boldsymbol{H}_{2D} : \boldsymbol{F}_{2D}. \tag{54}$$

Equations (52)-(53) enable to particularise the strain energy $e\,(\boldsymbol{\nabla}_0\boldsymbol{\phi})$ and its extended representation $W\,(\mathcal{V})$ in (5) to plane stress as

$$e\,(\boldsymbol{\nabla}_0\boldsymbol{\phi}) = \widetilde{e}\,(\boldsymbol{\nabla}_0\boldsymbol{\phi}_{2D}, \lambda_{33}) = \widetilde{W}\,(\mathcal{V}_{2D}, \lambda_{33})\,, \tag{55}$$

with $\mathcal{V}_{2D} = \{\boldsymbol{F}_{2D}, J_{2D}\}$. Making use of (52) and (53), the invariants $II_{\boldsymbol{F}}$ and $II_{\boldsymbol{H}}$ featuring in the constitutive model in (6) can be written in terms of the set $\{\mathcal{V}_{2D}, \lambda_{33}\}$ as

$$II_{\boldsymbol{F}} = II_{\boldsymbol{F}_{2D}} + \lambda_{33}^2; \qquad II_{\boldsymbol{H}} = \lambda_{33}^2 II_{\boldsymbol{F}_{2D}} + J_{2D}^2. \tag{56}$$

Making use of (56), the Mooney-Rivlin model in (6) can be particularised to plane stress as

$$\begin{aligned} \widetilde{W} = &\left(\frac{\mu_1}{2} + \lambda_{33}^2\frac{\mu_2}{2}\right) II_{\boldsymbol{F}_{2D}} + \frac{\mu_1}{2}\lambda_{33}^2 + \frac{\mu_2}{2}J_{2D}^2 \\ &- (\mu_1 + 2\mu_2)\,(\ln J_{2D} + \ln\lambda_{33}) + \frac{\kappa}{2}\,(J_{2D}\lambda_{33} - 1)^2 \\ &- \frac{3}{2}\,(\mu_1 + \mu_2)\,. \end{aligned} \tag{57}$$

Let $\delta\boldsymbol{\phi}_{2D}$ and $\Delta\boldsymbol{\phi}_{2D}$ denote virtual and incremental variations of the in-plane mapping $\boldsymbol{\phi}_{2D}$. The directional derivative of $\widetilde{e}\,(\boldsymbol{\nabla}_0\boldsymbol{\phi}_{2D}, \lambda_{33})$ with respect to possible virtual variations of the in-plane mapping is

$$D\widetilde{e}[\delta\boldsymbol{\phi}_{2D}] = \partial_{\boldsymbol{\nabla}_0\boldsymbol{\phi}_{2D}}\widetilde{e} : \boldsymbol{\nabla}_0\delta\boldsymbol{\phi}_{2D} + (\partial_{\lambda_{33}}\widetilde{e})\,D\lambda_{33}[\delta\boldsymbol{\phi}_{2D}], \tag{58}$$

where the second term on the right-hand side of (58) vanishes due to the plane stress assumption (refer to ***Remark 2*** below (60)). Making use of (58) and of the left-hand side of equation (8), it can be concluded that the first Piola-Kirchhoff stress tensor in plane stress is defined as

$$\boldsymbol{P}_{2D} = \partial_{\boldsymbol{\nabla}_0\boldsymbol{\phi}_{2D}}\widetilde{e}\,(\boldsymbol{\nabla}_0\boldsymbol{\phi}_{2D}, \lambda_{33})\,. \tag{59}$$

Remark 2. *The plane stress implies the out of plane component of the stress to vanish, i.e,*

$$\partial_{\lambda_{33}}\widetilde{e}\,(\boldsymbol{\nabla}_0\boldsymbol{\phi}, \lambda_{33}) = 0. \tag{60}$$

Generally, above equation (60) *is nonlinear and needs to be solved iteratively. In addition, the directional derivative of* λ_{33} *namely* $D\lambda_{33}[\delta\boldsymbol{\phi}_{2D}]$ *can be computed from the condition*

$$D\left(\partial_{\lambda_{33}}\widetilde{e}\,(\boldsymbol{\nabla}_0\boldsymbol{\phi}_{2D}, \lambda_{33})\right)[\delta\boldsymbol{\phi}_{2D}] = 0. \tag{61}$$

The directional derivative of the plane stress condition (61) *can be expanded as*

$$\begin{aligned} D\left(\partial_{\lambda_{33}}\widetilde{e}\,(\boldsymbol{\nabla}_0\boldsymbol{\phi}_{2D}, \lambda_{33})\right)[\delta\boldsymbol{\phi}_{2D}] = &\,\partial_{\lambda_{33}}\boldsymbol{P}_{2D} : \boldsymbol{\nabla}_0\delta\boldsymbol{\phi}_{2D} \\ &+ \left(\partial^2_{\lambda_{33}\lambda_{33}}\widetilde{e}\right) D\lambda_{33}[\delta\boldsymbol{\phi}_{2D}] = 0. \end{aligned} \tag{62}$$

Finally, $D\lambda_{33}[\delta\boldsymbol{\phi}_{2D}]$ *can be obtained from* (62) *as*

$$D\lambda_{33}[\delta\boldsymbol{\phi}_{2D}] = -\left(\partial^2_{\lambda_{33}\lambda_{33}}\widetilde{e}\right)^{-1}\left(\partial_{\lambda_{33}}\boldsymbol{P}_{2D} : \boldsymbol{\nabla}_0\delta\boldsymbol{\phi}_{2D}\right). \tag{63}$$

□

In the case of plane stress, the fourth order elasticity tensor $\boldsymbol{\mathcal{C}}$ emerges from the second directional derivative of the strain energy as

$$\begin{aligned} D^2\widetilde{e}[\delta\boldsymbol{\phi}_{2D}; \Delta\boldsymbol{\phi}_{2D}] = &\,\boldsymbol{\nabla}_0\delta\boldsymbol{\phi}_{2D} : \partial^2_{\boldsymbol{\nabla}_0\boldsymbol{\phi}_{2D}\boldsymbol{\nabla}_0\boldsymbol{\phi}_{2D}}\widetilde{e} : \boldsymbol{\nabla}_0\Delta\boldsymbol{\phi}_{2D} \\ &+ (\boldsymbol{\nabla}_0\delta\boldsymbol{\phi}_{2D} : \partial_{\lambda_{33}}\boldsymbol{P}_{2D})\,D\lambda_{33}[\Delta\boldsymbol{\phi}_{2D}]. \end{aligned} \tag{64}$$

Making use of (63) in (64) and comparison against (9) enables to obtain the following expression for the in-plane constitutive tensor $\boldsymbol{\mathcal{C}}_{2D}$

$$\boldsymbol{\mathcal{C}}_{2D} = \partial^2_{\boldsymbol{\nabla}_0\boldsymbol{\phi}_{2D}\boldsymbol{\nabla}_0\boldsymbol{\phi}_{2D}}\widetilde{e} - \left(\partial^2_{\lambda_{33}\lambda_{33}}\widetilde{e}\right)^{-1}\partial_{\lambda_{33}}\boldsymbol{P}_{2D}\otimes\partial_{\lambda_{33}}\boldsymbol{P}_{2D}. \tag{65}$$

Remark 3. *Proceeding similarly as in Remark 1, the following expression for the two-dimensional first Piola-Kirchhoff stress tensor* $\boldsymbol{P}_{2D}$ *can be obtained when considering the extended representation* $\widetilde{W}$ (55)

$$\boldsymbol{P}_{2D} = \partial_{\boldsymbol{F}_{2D}}\widetilde{W} + \partial_{J_{2D}}\widetilde{W}\boldsymbol{H}_{2D}. \tag{66}$$

Furthermore, the following expression (equivalent to that in (65)*) can be obtained for* $\boldsymbol{\mathcal{C}}_{2D}$ *in terms of the derivatives of* $\widetilde{W}$

$$\begin{aligned} \boldsymbol{\mathcal{C}}_{2D} = &\,\partial^2_{\boldsymbol{F}_{2D}\boldsymbol{F}_{2D}}\widetilde{W} + \partial^2_{J_{2D}J_{2D}}\widetilde{W}\boldsymbol{H}_{2D}\otimes\boldsymbol{H}_{2D} \\ &+ \partial^2_{\boldsymbol{F}_{2D}J_{2D}}\widetilde{W}\otimes\boldsymbol{H}_{2D} + \boldsymbol{H}\otimes\partial^2_{J_{2D}\boldsymbol{F}_{2D}}\widetilde{W} \\ &+ \partial_J\widetilde{W}\left(\boldsymbol{I}\otimes\boldsymbol{I} - \boldsymbol{\mathcal{I}}^T\right) - \left(\partial^2_{\lambda_{33}\lambda_{33}}\widetilde{W}\right)^{-1}\partial_{\lambda_{33}}\boldsymbol{P}_{2D}\otimes\partial_{\lambda_{33}}\boldsymbol{P}_{2D}, \end{aligned} \tag{67}$$

with

$$\partial_{\lambda_{33}}\boldsymbol{P}_{2D} = \partial^2_{\boldsymbol{F}_{2D}\lambda_{33}}\widetilde{W} + \partial^2_{J_{2D}\lambda_{33}}\widetilde{W}\boldsymbol{H}_{2D}. \tag{68}$$

□

References

Aage N, Andreassen E, Lazarov BS, Sigmund O (2017) Gigavoxel computational morphogenesis for structural design. Nature 550(84):84–86

Allaire G (2006) Conception optimale de structures. Springer

Allaire G, Jouve F, Toader A (2004) Structural optimization using sensitivity analysis and a level-set method. J Comput Phys 194(1):363–393

Bendsøe MP (1989) Optimal shape design as a material distribution problem. Struct Optim 1(4):193–202

Bendsoe MP, Kikuchi N (1988) Generating optimal topologies in structural design using a homogenization method. Computer Methods in Applied Mechanics and Engineering 71(2):197–224

de Boer R (1982) Vektor- und Tensorrechnung für Ingenieure. Springer-Verlag

Bonet J, Gil AJ, Lee CH, Aguirre M, Ortigosa R (2015a) A first order hyperbolic framework for large strain computational solid dynamics - Part I: Total Lagrangian isothermal elasticity. Comput Methods Appl Mech Eng 283(0):689–732

Bonet J, Gil AJ, Ortigosa R (2015b) A computational framework for polyconvex large strain elasticity. Comput Methods Appl Mech Eng 283:1061–1094

Bonet J, Gil AJ, Ortigosa R (2016a) On a tensor cross product based formulation of large strain solid mechanics. Int J Solids Struct 84:49–63

Bonet J, Gil AJ, Wood RD (2016b) Nonlinear Continuum Mechanics for Finite Element Analysis: Statics. Cambridge University Press

Bruns TE, Tortorelli DA (2003) An element removal and reintroduction strategy for the topology optimization of structures and compliant mechanisms. International Journal for Numerical Methods in Engineering 57:1413–1430

Burden RL, Faires JD, Burden AM (2015) Numerical Analysis. Cengage Learning

Burger M, Stainko R (2006) Phase-Field Relaxation of Topology Optimization with Local Stress Constraints. SIAM J Control Optim 45(4):1447–1466

Chen F, Wang Y, Wang M, Zhang Y (2017) Topology optimization of hyperelastic structures using a level set method. Journal of Computational Physics 351:437 – 454

Geiss M, Boddeti N, Weeger O, Maute K, Dunn M (2018) Combined level-set-xfem-density topology optimization of 4d printed structures undergoing large deformation. ASME J Mech Des

Gursel A (2018) Softer is harder: What differentiates soft robotics from hard robotics? MRS Advances 3(28):15571568, DOI 10.1557/adv.2018.159

Ha S, Cho S (2008) Level set based topological shape optimization of geometrically nonlinear structures using unstructured mesh. Comput Struct 86(13):1447–1455

Hesch C, Gil A, Ortigosa R, Dittmann M, Bilgen C, Betsch P, Franke M, Janz A, Weinberg K (2017) A framework for polyconvex large strain phase-field methods to fracture. Comput Methods Appl Mech Eng 317:649–683

Jensen JS, Sigmund O (2011) Topology optimization for nanophotonics. Laser Photonics Rev 5(2):308–321

Jung D, Gea H (2004) Topology optimization of nonlinear structures. Finite Elements in Analysis and Design 40(11):1417–1427

Lahuerta R, Simões E, Campello E, Pimenta P, Silva E (2013) Towards the stabilization of the low density elements in topology optimization with large deformation. Computational Mechanics 52(4):779–797

Laurain A (2018) A level set-based structural optimization code using FEniCS. Struct Multidiscipl Optim 58(3):1311–1334

Liu L, Xing J, Yang Q, Luo Y (2017) Design of large-displacement compliant mechanisms by topology optimization incorporating modified additive hyperelasticity technique. Mathematical Problems in Engineering

Munk DJ, Vio GA, Steven GP (2015) Topology and shape optimization methods using evolutionary algorithms: a review. Struct Multidiscip Optim 52(3):613–631

Norato JA, Bendsøe MP, Haber RB, Tortorelli DA (2007) A topological derivative method for topology optimization. Struct Multidiscip Optim 33(4–5):375–386

Ortigosa R, Gil AJ (2017) A computational framework for incompressible electromechanics based on convex multivariable strain energies for geometrically exact shell theory. Comput Methods Appl Mech Eng 317:792–816

Ortigosa R, Gil AJ, Bonet J, Hesch C (2015) A computational framework for polyconvex large strain elasticity for geometrically exact beam theory. Comput Mech 57:277–303

Osher S, Sethian JA (1988) Front propagation with curvature dependent speed: Algorithms based on Hamilton-Jacobi formulations. J Comp Phys 78:12–49

Poya R, Sevilla R, Gil AJ (2016) A unified approach for a posteriori high-order curved mesh generation using solid mechanics. Comput Mech 58(3):457–490

Rus D, Tolley M (2015) Design, fabrication and control of soft robots. Nature 521:467–475

Sethian J, Wiegmann A (2000) Structural boundary design via level set and immersed interface methods. J Comput Phys 163(1):489–528

Sigmund O, Maute K (2013) Topology optimization approaches a comparative review. Structural and Multidisciplinary Optimization 48(6):1031–1055

Sokolowski J, Zochowski A (1999) On the Topological Derivative in Shape Optimization. SIAM J Control Optim 37(4):1251– 1272

Takezawa A, Nishiwaki S, Kitamura M (2010) Shape and topology optimization based on the phase field method and sensitivity analysis. J Comput Phys 229(7):2697–2718

Wallin T, Pikul J, Shepherd R (2018) 3d printing of soft robotic systems. Nat Rev Mater 3:84–100

Wang F, Lazarov BS, Sigmund O, Jensen JS (2014) Towards the stabilization of the low density elements in topology optimization with large deformation. Computer Methods in Applied Mechanics and Engineering 276:453–472

Wang M, Wang X, Guo D (2003) A level-set method for structural topology optimization. Comput Meth Appl Mech Eng 192(1–2):227–246

Wehner M, Truby R, Fitzgerald D, Mosadegh B, Whitesides G, Lewis J, Wood R (2016) An integrated design and fabrication strategy for entirely soft, autonomous robots. Nature 536:451–455

Zhou M, Rozvany GIN (1991) The COC algorithm, part II: topological, geometrical and generalized shape optimization. Comput Methods Appl Mech Eng 89(1–3):309–336

Zhu JH, Zhang WH, Xia L (2016) Topology optimization in aircraft and aerospace structures design. Arch Comput Meth Eng 23(4):595–622